

# THE VLBA GALACTIC PLANE SURVEY — VGAPS

L. PETROV

ADNET Systems Inc./NASA GSFC, Greenbelt, MD 20771, USA

Y. Y. KOVALEV

Astro Space Center of Lebedev Physical Institute, Profsoyuznaya 84/32, 117997 Moscow, Russia and  
National Radio Astronomy Observatory, P.O. Box 2, Green Bank, WV 24944, USA

E. B. FOMALONT

National Radio Astronomy Observatory, 520 Edgemont Road, Charlottesville, VA 22903–2475, USA

D. GORDON

NVI Inc./NASA GSFC, Code 698.2 Greenbelt, MD 20771, USA

(Received 2011 January 6; Accepted 2011 May 1; Published 2011 June 22)

## ABSTRACT

This paper presents accurate absolute positions from a 24 GHz Very Long Baseline Array (VLBA) search for compact extragalactic sources in an area where the density of known calibrators with precise coordinates is low. The goals were to identify additional sources suitable for use as phase calibrators for galactic sources, determine their precise positions, and produce radio images. In order to achieve these goals, we developed a new software package, *PLIMA*, for determining group delays from wide-band data with much lower detection limit. With the use of *PLIMA* we have detected 327 sources out of 487 targets observed in three 24 hour VLBA experiments. Among the 327 detected objects, 176 are within 10 degrees of the Galactic plane. This VGaPS catalogue of source positions, plots of correlated flux density versus projected baseline length, contour plots, as well as weighted CLEAN images and calibrated visibility data in FITS format, are available on the Web at <http://astrogeo.org/vgaps>. Approximately one half of objects from the 24 GHz catalogue were observed at dual band 8.6 GHz and 2.3 GHz experiments. Position differences at 24 GHz versus 8.6/2.3 GHz for all but two objects on average are strictly within reported uncertainties. We found that for two objects with complex structure positions at different frequencies correspond to different components of a source.

*Subject headings:* astrometry — catalogues — surveys

## 1. INTRODUCTION

The method of very long baseline interferometry (VLBI), first proposed by Matveenko et al. (1965), has numerous applications in the areas of high resolution imaging, differential astrometry, absolute astrometry, space geodesy, and space navigation. Because the turbulence in the neutral atmosphere and ionospheric fluctuations set a limit of coherent averaging at typically 1 to 10 minutes, depending on frequency, the detection of weak sources that require longer integration is not possible.

To overcome this limitation, the majority of VLBI observations are made in phase referencing mode: the telescopes of the array slew rapidly between a weak target and a nearby strong calibrator. The phase changes of the calibrator trace the fluctuations in the atmosphere, and when they are subtracted from the phase of the target, the residual phases are essentially free from fluctuations caused by the atmosphere, and the target integration time can be extended almost indefinitely, enabling detection and imaging of weak objects. This technique is called phase-referencing.

The technique of phase referencing allows also to determine the precise differential position of a target with respect

to a calibrator with accuracy reaching 0.05 mas or better, even with moderate signal-to-noise ratio (SNR). The advantage of differential astrometry over absolute astrometry is that the contribution of unaccounted propagation delays and errors in station positions is diluted by a factor of the target-to-source separation in radians. Either the target or calibrator may be observed in a narrow band.

The ability to image weak sources and determine their positions accurately with respect to a nearby calibrator have made phase referencing very popular. According to Wrobel (2009), in 2003–2008, 63% of VLBA observations used this technique. However, to make phase referencing possible, a dense catalogue of phase calibrators is needed such that a suitable calibrator will be found within 2–3° of any target. And for precise differential astrometry, the calibrator position accuracy of a few milliarcsecond is needed. Efforts to create such a catalogue of calibrators commenced in the 1980s under the NASA's Crustal Dynamic Project program (Ryan & Clark 1987) that ultimately resulted in the ICRF catalogue of 608 sources (Ma et al. 1998). Later, over 6000 sources were observed in the framework of the VLBA Calibrator Survey (VCS) program (Beasley et al. 2002, Fomalont et al. 2003, Petrov et al. 2005, 2006, Kovalev et al. 2007, Petrov et al. 2007c), the VLBA RDV program (Petrov et al. 2009), and the continuing Australian Long Baseline Array Calibrator Survey (LCS) program (Petrov et al. 2011). By the end of 2010, the number of known calibrators with position accuracies better

Leonid.Petrov@lpetrov.net  
yyk@asc.rssi.ru  
efomalont@nrao.edu  
David.Gordon-1@nasa.gov

than 5 mas surpassed 4600. The probability of finding a calibrator within  $2^\circ$  of any direction is currently 64%, and within  $3^\circ$  is 90%. However, the distribution of calibrators is not uniform on the sky due to several factors: the large scale structure of the Universe; the location of most observing stations in the northern hemisphere; and obscuration and confusion within  $5^\circ$  of the Galactic plane.

Finding calibrators in the Galactic plane region is especially difficult for several reasons. First, the region is filled with many galactic objects, and surveys from single antennas or km-sized arrays, which are needed to find calibrator candidates, avoid this region; for example JVAS (Wrobel et al. 1998) and AT20G (Murphy et al. 2010). Therefore, the pool of available candidates is limited near the plane. Second, many potential candidates with flat spectra are extended galactic objects, such as planetary nebulae or HII regions, that cannot be detected by VLBI. Finally, the apparent angular size of extragalactic objects observed through high plasma density near the Galactic plane are broadened by Galactic scattering, and cannot be detected at low frequencies on baselines longer than several thousand kilometers.

Nevertheless, a dense grid of calibrators in the Galactic plane is needed for studies of compact galactic objects in both continuum emission (pulsars, X-ray binaries) and line emission (e.g. water masers, methanol masers, Hydrogen absorption). Some extragalactic sources near the Galactic plane have been associated with *Fermi*-detected  $\gamma$ -ray objects (Abdo et al. 2010a,b) only through VLBI calibrator surveys as it was suggested and successfully shown by Kovalev (2009).

In order to increase the density of calibrators in the Galactic plane and to search for suitable calibrators within  $2^\circ$  of known water masers, we developed an observing strategy that combine the VERA and VLBA arrays. First, we systematically screened 2462 sources with declinations  $> -40^\circ$  using the 4-station VLBI array VERA (Honma et al. 2003) at 22 GHz (K-band) by observing each object in two 120-second long scans. We detected 533 objects, 180 of them new at K-band, and these results are given in Petrov et al. (2007b). Since precise determination of parallaxes and proper motions of sources with water-maser emission is one of the main targets of the VERA project, potential calibrators near known water masers were preferentially included in the observations.

This paper describes the follow-up VLBA observations at 24 GHz of 487 radio sources in order to determine their precise positions and images. We denote these observations as the VLBA Galactic Plane Survey (VGaPS), and the results of this observing campaign are described in this paper. VLBA observations, source selection and the scheduling algorithm are given in section §2. The data analysis procedure is presented in §3. For analysis of these observations we have developed a new approach for wide-band fringe search and astrometric analysis which is described in detail in §3.2. The validation of the results made with the new approach is given in §4. The images are described in section §6, the source position catalog is listed in §7, and the K- and S/X-band astrometric VLBI positions are compared in §8. The results are summarized in section §9.

## 2. SOURCE SELECTION AND OBSERVATIONS

The VLBA observations were made at 24 GHz for several reasons. First, Galactic scattering at low frequencies broadens images and degrades source positions. Even at the frequency of 8.6 GHz, many calibrators near the Galactic plane are too broadened to be useful. Second, many galactic radio

targets are associated with H<sub>2</sub>O maser emission at 22.5 GHz. Since the correlated flux density of calibrators generally decreases with increasing frequency, a good calibrator at 2.3 and 8.6 GHz may not be sufficiently compact or bright for use at 22 GHz. Third, source positions at 22 GHz may not necessarily be the same as those at 8.6 GHz because of the effects of frequency dependent source structure, especially for multi-component objects, and because of frequency dependent core shifts (e.g., Lobanov 1998, Kovalev et al. 2008, Sokolovsky et al. 2011).

We considered the task of extending the pool of calibrators for Galactic astrometry more broadly: not only to increase the list of compact extragalactic radio sources within  $10^\circ$  of the Galactic plane, but also to re-observe known sources at K-band that are either in the Galactic plane or close to known masers at higher galactic latitudes. Water masers are the main target of the VERA project, and determination of their parallaxes and proper motions is important for studying the three-dimensional structure and dynamics of the Galaxy's disk and bulge, and for revealing the true shape of the bulge and spiral arms, its precise rotation curve and the distribution of dark matter. Dual-beam K-band VERA observations require calibrators with positions known to the milliarcsec level within  $2.^\circ2$  of the target.

### 2.1. Source selection

VLBI can detect emission only from a compact component of a source, which should be bright enough to be detected above the noise background. Chances to find a radio source sufficiently compact for VLBI detection are significantly enhanced if information about source spectra is available. For a majority of sources with flat spectrum, i.e. with the spectral index  $\alpha > -0.5$  ( $S \sim f^\alpha$ ), synchrotron emission from a compact core often dominates, so such sources are often compact. In regions more than  $10^\circ$  from the Galactic plane, comparison of surveys at different frequencies can be used to select the sources with flat spectra. However, in the crowded Galactic plane, source misidentification and confusion from surveys at different frequencies often result in ambiguous information about a source spectrum. Also, there are many extended sources with thermal emission, such as planetary nebulae and HII regions, that have flat spectrum but are too extended for VLBI detection.

To determine if a candidate source was sufficiently strong and compact to be a VLBI calibrator, we first used the VERA array at 22 GHz (Petrov et al. 2007b). In the survey  $\sim 1400$  objects within  $6^\circ$  of the Galactic plane and  $\sim 1000$  objects within  $2^\circ$  of known maser sources outside the Galactic plane were observed with the four-element VERA array at baselines of 1000–2000 km long in two scans each, and approximately 20% were detected. Among the 533 detected sources, 305 objects are with galactic latitude  $|b| < 10^\circ$ , and 228 objects are with  $|b| > 10^\circ$ . The list of detected sources included all objects with the probability of false detection  $< 0.1$ . These objects formed the first set of candidate calibrators.

We also added 239 objects in the Galactic plane and 44 objects outside Galactic plane, selected on the basis of their spectra using the Astrophysical CATALOGs support System CATS (Verkhodanov et al. 2005). This database currently includes catalogues from 395 radio astronomy surveys. We selected all entries with sources within a  $20''$ -radius and with measurements of flux density at least at three frequencies in the range of 1.4–100 GHz. We fit a straight line to the logarithm of the spectrum and then estimated the spectral index

and the flux density extrapolated to 24 GHz. We selected 451 objects with extrapolated correlated flux densities at K-band  $> 200$  mJy, spectral index flatter than  $-0.5$  and  $|b| < 10^\circ$ . Then, we scrutinized this list and removed sources within  $30''$  of known planetary nebulae or HII regions and sources with anomalous spectra that indicated a possible misidentification. The remaining list was added to the pool of calibrators. This list contained also Sagittarius A\* since it has never before been observed with VLBI in the absolute astrometry mode.

This set of sources formed the pool of 816 candidate objects to be followed-up with the VLBA. Because of the large number of candidate objects, a priority from 1 to 4 was assigned to each source. The first priority was given to 180 new sources with correlated flux densities in the range 100–300 mJy detected with VERA that have never been observed with VLBI before. The second was given to sources in the Galactic plane detected with VERA; the third was given to other sources detected with VERA; and the least priority was given to sources outside the Galactic plane not detected with VERA. All new sources detected with VERA were scheduled. Source outside of the Galactic plane were included for logistical reasons. Since the Galactic plane has an inclination with respect to the equator of  $62^\circ.6$ , the density of candidate sources near the Galactic plane is a non-uniform function of right ascensions. We thus included sources outside the Galactic plane in the right ascension regions that had significantly fewer candidate sources than others in order to avoid gaps in the schedules.

In addition to the target sources, we also selected 56 objects from the K/Q survey (Lanyi et al. 2010) to serve as amplitude and atmosphere calibrators. These are the brightest sources at K-band with precisely known positions and publicly available images in FITS-format.

## 2.2. Scheduling algorithm

A sufficiently good preliminary VLBA observing schedule for three 24-hour sessions was prepared automatically. Then it was manually adjusted in order to produce a more efficient final schedule.

The three sets of information needed in order to compile the schedule were: 1) the list of the 816 target sources with their J2000 positions and priority level; 2) the list of the 56 calibration sources at 24 GHz; and 3) the two or three sidereal times ranges (at the array center at station PIETOWN) that each source should be observed. These times were a function of the source declination. For example, a source with  $\delta > 50^\circ$  could be observed three times with very flexible time ranges; whereas, a source with  $\delta < -35^\circ$ , must have tight ranges in order to be observed by at least 8 VLBA antennas at an elevation higher than ten degrees.

The scheduling goal was to observe each source for three scans of 120 seconds length, unless it was south of declination  $-25^\circ$ , in which case only two scans were scheduled. With an average overhead of about 45 sec between sources, about 1550 scans over the three days (72 hours) could be scheduled. Every 90 minutes, four scans were reserved for atmosphere calibrators. The algorithm then began filling in observing slots, taking the highest priority sources first, and those at the lowest declinations, since these have minimal scheduling flexibility. The algorithm scheduled sources that were relatively close in the sky in order to minimize slew times, which can be as long as three minutes.

The slots containing the calibrators were chosen in order to maximize the range of elevations for the VLBA antennas. In practice, this meant maximizing elevations of observed

**Table 1**  
VLBA Target Sources from VERA Observations

| group                | pool | scheduled | detected | ratio |
|----------------------|------|-----------|----------|-------|
| Galactic, VERA       | 305  | 184       | 140      | 76%   |
| Non-galactic, VERA   | 228  | 151       | 133      | 88%   |
| Galactic others      | 239  | 108       | 36       | 33%   |
| Non-galactic, others | 44   | 44        | 15       | 34%   |
| Total                | 816  | 487       | 327      | 67%   |

sources at SC-VLBA, MK-VLBA and PIETOWN. It was important to have one low elevation observation for all telescopes, and this could be scheduled by observing a source either in the far north and/or in the far south. All three days were scheduled at the same time, since it did not matter on which day any of the three sidereal time slots occurred for a source.

The final schedule optimization was done ‘by hand’ and consisted of several steps. First, some sources could be placed in only one or two slots and would have to be removed if another slot could not be found. Since about 10% of the slots could not be filled using the automatic algorithm because the source list was not uniformly distributed over the sky, additional slots were usually found to complete a source’s schedule requirement. This often meant bending some of the rules or moving calibration sources or blocks by five to fifteen minutes. In regions where the target source density was large, scan integrations were decreased from 120 sec to 110 sec. All sources with priority 1 were included.

The next stage insured that the calibration scans were optimized in order to obtain good elevation coverage for the antennas. The purpose of these observations was 1) to serve as amplitude and bandpass calibrators; 2) to improve robustness of estimates of the path delay in the neutral atmosphere; and 3) to tie the source positions of new sources to existing catalogues, such as the ICRF catalogue (Ma et al. 1998). The final stage of optimization tweaked the observing schedule in obvious ways in order to save slewing time since the scheduling algorithm did not minimize slew times, and because of the above adjustments to insure proper observing coverage for each source. The schedule for each session was then carefully checked using the NRAO SCHED program to insure that each scan had sufficient integration time, and no more than one of the antennas was below ten degree elevation (except for sources south of  $-35^\circ$ ).

The results of the scheduling and ultimate detection for each priority group is given in Table 1. The number of target sources selected in each group is given in column 2, those scheduled in column 3, those detected by the VLBA in column 4, and the detection rate in the last column. The first two groups are sources detected in VERA Fringe Search Survey, the last two groups contain other objects. The table does not include the 56 sources used as atmosphere calibrators.

## 2.3. Observations

The VGaPS observations were carried out in three 24 hour observing sessions at the VLBA on 2006 June 04, 2006 June 11, and 2006 October 20. Each target source was observed in several scans: 3 sources in 1 scan, 356 sources in 2 scans, 1 source in 3 scans, 124 in 4 scans and 3 sources in 5 scans. The scan durations were 100–120 seconds. In total, antennas spent 57% of time on target sources. In addition to these target objects, 56 strong sources previously observed at K-band were taken from the astrometric and geodetic catalogue



**Table 2**  
The lower edge IF frequencies (in GHz)

|     |          |
|-----|----------|
| IF1 | 24.20957 |
| IF2 | 24.22257 |
| IF3 | 24.26157 |
| IF4 | 24.33957 |
| IF5 | 24.48257 |
| IF6 | 24.58657 |
| IF7 | 24.65157 |
| IF8 | 24.67757 |

2004f\_astro<sup>1</sup>.

The data digitized at four levels were recorded with the rate of 256 Mbit/s in eight 8 MHz wide intermediate frequencies (IF) bands spread over a bandwidth of 476 MHz (Table 2). The frequencies were selected to minimize the amplitude of sidelobes of the Fourier transform of the bandpass.

### 3. DATA ANALYSIS

The data were correlated in Socorro on the VLBA hardware correlator. The correlator output contains the complex spectra of the autocorrelation function and the spectrum of the cross-correlation function for each accumulation period. The accumulation period was chosen to be 0.131072 s, and the spectral resolution was set to 0.5 MHz, i.e. 16 spectral channels per IF.

After correlation, the data were stored in a file compliant with the FITS-IDI specifications (Eric Greisen, NRAO memo N114<sup>2</sup>). Small a priori amplitude corrections were applied; bad data were flagged (sometimes bad data are not found until later processing); and the definitions of the reference frequencies were modified.

Further data analysis involves computation of group delays for each scan and each baseline, computation of theoretical path delay, and then fitting parameters of the linear model into the differences between the observed and theoretical delays using least squares (LSQ).

#### 3.1. Traditional narrow-band fringe fitting algorithm

The data set then contains 128 data streams for each of the 45 baselines if all ten VLBA antennas are operating: 8 IF's, each with 16 equally-space frequency channels. After the complex bandpass calibration, the phase difference among all of the frequency streams remains unchanged, and the relevant residual phase parameters associated with any scan are 1) the residual phase at the scan midpoint, 2) the average group delay (phase gradient with frequency), and 3) the average delay rate (delay gradient with time), for each antenna. These parameters are called the *residual phase terms*. These parameters are estimated with a fringe fitting procedure. Generally, one antenna is chosen as the reference — a well-behaved one near the array center — so that set of a residual phase terms are associated for each scan and all other antennas. These parameters are functions of many astrometric quantities (source position, site positions, antenna-based tropospheric path delays, Earth Orientation parameters, etc), which can be determined from analysis systems like Calc/Solve from data obtained from carefully prepared observing schedules. Source structure and dispersive phase effects (e.g. ionosphere) produce a non-linear phase/frequency relationship.

The algorithm that determines the residual phase terms is implemented in the AIPS task FRING, and in the past, all VLBA observations under the absolute astrometry and geodesy programs, such as VCS, RDV, and K/Q, were processed with use of this software (Greisen 1988). When IFs are spread over a wide band with gaps, the AIPS algorithm determines the residual phase in two steps: first, for each of the 8 IF's the residual phase, single-band group delay and rates are independently obtained. Then, the residual phases of each IF are fit to a linear phase versus frequency term to produce the group delay, using AIPS program MBDLY. This procedure is described in detail in Petrov et al. (2009).

#### 3.2. Wide-band baseline-based fringe fitting algorithm

The two-step approach has a substantial shortcoming: it requires fringe detection for each individual IF independently within a narrow band. Using all  $N$  IFs simultaneously for coherent averaging, we can detect a source with the amplitude  $\sqrt{N}$  smaller than using only one IF. This degradation of the detection limit does not pose a problem for most geodesy observations, or for absolute astrometry of bright sources, since the target SNR is usually very high, but it impacts significantly absolute astrometric experiments of weak sources. The traditional AIPS algorithm did not detect a sizeable fraction of the sources observed in the VGaPS experiment.

This limitation motivated us to develop an advanced algorithm for wide-band fringe fitting across all of the IF's within the band. For logistical reasons, instead of augmenting AIPS with the new task, we decided to develop from scratch the new software package called *PLIMA*<sup>3</sup> that is supposed to replace the AIPS for processing absolute astronomy and geodesy experiments. Here we outline the method of wide-band fringe search used for processing this experiment.

##### 3.2.1. Spectrum re-normalization

Digitization of the input signal and its processing with a digital correlator causes an amplitude distortion with respect to an ideal analogue system. As documented by Kogan (1995), many effects distort both cross-correlation and auto-correlation spectrum exactly the same way. Therefore, if we divide the cross-correlation spectrum by the auto-correlation spectrum averaged over time and over frequencies within each IF, we will remove these distortions. However, there are two effects that affect cross- and auto-spectrum differently because the amplitude of the cross-spectrum is very low, and the amplitude of the auto-correlation spectrum is close to 1.

The non-linear amplitude distortion of the digitized signal was studied in depth by Kogan (1998) who derived a general expression for the correlation coefficient of the digitized signal as a function of the correlation coefficient of the hypothetical analogue signal. In the absence of fringe stopping, the output correlation coefficient  $\rho_{out}$  is expressed via the correla-

<sup>1</sup> <http://astrogeo.org/rfc>

<sup>2</sup> Available at <ftp://ftp.aoc.nrao.edu/pub/software/aips/> and <http://www.nrao.edu/aips/>

<sup>3</sup> Available at <http://www.nrao.edu/aips/pima/>

tion coefficient for an analogue case  $\rho$  as

$$\begin{aligned} \rho_{out} = & 2\kappa \int_0^\rho \frac{1}{\sqrt{1-\rho^2}} d\rho \\ & + 2\kappa(n-1) \int_0^\rho \frac{1}{\sqrt{1-\rho^2}} \left( e^{-\frac{v_1^2}{2(1-\rho^2)}} + e^{-\frac{v_2^2}{2(1-\rho^2)}} \right) d\rho \\ & + \kappa(n-1)^2 \int_0^\rho \frac{1}{\sqrt{1-\rho^2}} \left( e^{-\frac{v_1^2-2\rho v_1 v_2+v_2^2}{2(1-\rho^2)}} + e^{-\frac{v_1^2+2\rho v_1 v_2+v_2^2}{2(1-\rho^2)}} \right) d\rho, \end{aligned} \quad (1)$$

where  $\kappa$  is the normalization coefficient,  $n$  is the ratio of two level of quantization,  $v_1$  and  $v_2$  are the dimensionless digitizer levels in units of variance of the input signal. Their numerical values compiled from the paper of Kogan (1993) are presented in table 3.

**Table 3**

Numerical coefficients in integral 1 for three cases of the number of bits per sample: (1,1), (1,2), (2,2)

|       | $n$    | $v_1$  | $v_2$  | $\kappa$ |
|-------|--------|--------|--------|----------|
| (1,1) | 1.0    | 0.0    | 0.0    | 0.3803   |
| (1,2) | 3.3359 | 0.0    | 0.9816 | 0.05415  |
| (2,2) | 3.3359 | 0.9816 | 0.9816 | 0.07394  |

When  $\rho \ll 1$ , the dependence  $\rho_{out}(\rho)$  becomes linear:  $\rho_{out} \approx 2/\pi \cdot \rho \approx 0.6366\rho$  for the case of 1-bit sampling, and  $\rho_{out} \approx 0.8825\rho$  for the case of 2-bit sampling. Therefore, distortion of the cross-spectrum is proportional to  $\rho_{out}/\rho$ , and dividing the cross-spectrum by 0.6366 or 0.8825 we eliminate the distortion of the fringe amplitude introduced by the digitization.

However, the amplitude of the autocorrelation spectrum is close to 1, and we cannot ignore non-linearity of  $\rho_{out}(\rho)$ . To correct the autocorrelation spectrum for digitization distortion, we follow the procedure outlined by Kogan (1995). First, the auto-correlation is inverse Fourier transformed. It should be noted that the correlator provides the autocorrelation for  $N$  spectral channels for non-negative frequencies from 0 to  $N-1$ . We restore the autocorrelation at the  $N$ -th channel by linear extrapolation using the  $N-2$ -th and  $N-1$ -th values of the spectrum and set the spectrum for  $N-1$  negative frequencies to zero. The dimension of the Fourier transform is  $2N$ . Second, the result of the transformation, the auto-correlation coefficient versus time lag, is de-tapered, i.e. divided by the self-convolution of the weighting function. The VLBA correlator normally uses uniform weighting, i.e. uses weight 1 for all points. The self-convolution of the uniform weighting is a triangle function  $\wedge(i)$ :

$$\wedge(i) = \begin{cases} \frac{1}{N}(N-|i|) & \text{if } |i| < N \\ 0 & \text{otherwise} \end{cases}$$

Third, the correlation function is divided by its maximum that is found at the zero lag. Fourth, each correlation coefficient is divided by  $\rho_{out}(\rho)$ . Fifth, the correlation function is multiplied back by the stored value at the zero lag. Sixth, the correlation function is again tapered by multiplying it by  $\wedge(i)$ . Finally, we perform the Fourier transform of the corrected correlation function and get the re-normalized auto-spectrum, free from digitization distortion. The square root of the product of the auto-correlation spectra from two stations of a baseline, averaged over time and frequency within

each IF, gives us an estimate of the fringe amplitude scale factor. But before dividing the cross-correlation spectrum by this scale-factor we have to take into account a specific effect of the hardware VLBA correlator<sup>4</sup>. An insufficient number of bits in internal correlator registers resulted in a decrease of the amplitude when its is large, and when it happens, the autocorrelation spectra are corrupted. Kogan (1993) suggested the following model for accounting for this effect:

$$F = 1 + \frac{w}{4SAV_s}, \quad (2)$$

where  $w$  is the weight of the spectrum data equal to the ratio of processed samples to the total number of samples in an accumulation period,  $A$  is the accumulation period length,  $S$  is 2 when the correlator processed single polarization data and 1 if both polarizations were correlated, and  $V_s$  is the visibility scale factor provided by the correlator. We divide the autocorrelation spectrum by the  $F$  factor.

### 3.2.2. Coarse fringe search

The correlator output provides autocorrelation and cross-correlation spectra for each pair of baselines and each scan. The cross-correlation spectrum is computed at a uniform two-dimensional grid of accumulation periods and frequencies and is accompanied with weights that are the ratio of the number of processed samples in each accumulation period to the nominal number of samples.

The fringe fitting procedure searches for phase delay  $\tau_p$ , phase delay rate  $\dot{\tau}_p$ , group delay  $\tau_g$ , and its time derivative  $\dot{\tau}_g$  that correct their a priori values used by the correlator model in such a way that the coherent sum of weighted complex cross-correlation samples  $c_{kj}$

$$C(\tau_p, \tau_g, \dot{\tau}_p, \dot{\tau}_g) = \sum_k \sum_j c_{kj} w_{kj} \times e^{i(\omega_0 \tau_p + \omega_0 \dot{\tau}_p(t_k - t_0) + (\omega_j - \omega_0) \tau_g + (\omega_j - \omega_0) \dot{\tau}_g(t_k - t_0))} \quad (3)$$

reaches the maximum amplitude. Index  $k$  runs over time, and index  $j$  runs over frequencies.  $\omega_0$  and  $t_0$  denote angular reference frequency within the band and the reference time within a scan and  $w_{kj}$  are weights. Function  $C(\tau_p, \tau_g, \dot{\tau}_p, \dot{\tau}_g)$  is essentially non-linear, and we need a really good starting value in order to find the global maximum by traditional optimization algorithms. We can notice that term  $2\pi\omega_0\tau_p$  in expression 3 does not depend on the summation indexes, and  $\dot{\tau}_g$  is usually small. Therefore, for the purpose of coarse fringe search we simplify expression 3 to

$$C(\tau_p, \tau_g, \dot{\tau}_p) e^{-i2\pi\omega_0\tau_p} \approx \sum_k \sum_j c_{kj} \times e^{i(\omega_0 \dot{\tau}_p(t_k - t_0) + (\omega_j - \omega_0) \tau_g)}. \quad (4)$$

For the search of the maximum, the trial functions  $C(\tau_p, \tau_g, \dot{\tau}_p)$  are computed on a dense grid of the search space  $\tau_g, \dot{\tau}_p$ . It follows immediately from expression 4 that  $|C| = |\mathcal{F}(c_{kj})|$ , where  $\mathcal{F}$  denotes the two dimensional Fourier transform.

The first step of the coarse fringe search is to compute the two-dimensional Fast Fourier Transform (FFT) of the matrix of the cross-correlation spectrum. The first dimension of the matrix runs over time, the second dimension runs over frequency. The sampling intervals are  $\Delta t/\beta$  and  $\Delta f/\gamma$  where

<sup>4</sup> The new VLBA software DiFX correlator does not have this problem.

$\Delta t$  and  $\Delta f$  are the duration of the accumulation period and the spectral resolution respectively, and  $\beta$  and  $\gamma$  are integer oversampling factors. The elements of the matrix which do not have measurements or have discarded measurements are padded with zeroes. The dimensions of the matrix are chosen to have the power of 2 for gaining the maximum performance of the FFT numerical algorithm.

The oversampling factors greater than 1 are used for mitigation of amplitude losses. The FFT produces the estimates of  $|C|$  at a discrete grid of group delays and delay rates. If the maximum of the amplitude of the coherent sum of the cross correlation function samples falls at group delays and delay rates between the nodes of the grid, its magnitude will be greater than the amplitude of  $|C|$  at the nearest grid point by a factor  $L$ .

The amplitude loss factor  $L$  at the coarse search matrix is the integral average over time and frequency:

$$L = \frac{1}{t_s} \int_{-t_s/2}^{t_s/2} \cos 2\pi \left( \omega_0 \tau_p - \frac{k}{\beta t_s} \right) t dt \times \frac{1}{f_b} \int_{-f_b/2}^{f_b/2} \cos 2\pi \left( \omega_0 \tau_g - \frac{l}{\gamma f_b} \right) f df, \quad (5)$$

where  $k$  and  $l$  are indexes of the nearest grid nodes,  $t_s$  is the scan duration,  $f_b$  is the total bandwidth. The integral 5 is easily evaluated analytically, and the maximum losses  $L = \text{sinc}(\pi/(2\beta)) \cdot \text{sinc}(\pi/(2\gamma))$  are achieved when  $\tau_p$  and  $\tau_g$  happen to be just between grid nodes. In the case when the oversampling factor is 1,  $L = 4/\pi^2 \approx 0.405$ . That loss factor effectively raises the detection limit by  $1/L = 2.467$  in the worst case. We used the grid  $4096 \times 4096$  which corresponds to  $\beta = 4, \gamma = 4$  for  $t_s = 120$  s,  $f_b = 476$  MHz. Therefore, the maximum loss factor for our experiment is 0.959, which results in raising the detection limit by no more than 4.1%.

The group delay and delay rate that correspond to the maximum of the discrete Fourier transform of the cross-correlation matrix provide the coarse estimates of group delay and delay rate. Their accuracy depends on the grid resolution. The next step is to refine their estimates. The first stage of the fine search is an iterative procedure that computes  $|C|$  at a progressively finer three-dimensional grid at the close vicinity of the maximum using the discrete 3D Fourier transform. The third dimension is group delay rate, omitted during the coarse search. Dimensions of the transform for group delay, phase delay rate, group delay rate are 3, 3, and 9 respectively. At the first step of iterations, the grid runs over  $\pm 1$  element of the coarse grid for group delays and phase delay rates and in the range  $\pm 2 \cdot 10^{-11}$  for group delay rate. After each step of iterations, the grid centered around the maximum element shrinks its step by 2. In total, 8 iterations are run. The phase of the coherent sum of cross correlation function determined with the iterative procedure according to expression 4 is the fringe phase with the opposite sign.

### 3.2.3. The probability of false detection

The significance of the fringe amplitude depends on the level of noise. In the absence of signal, the amplitude of the cross correlation function  $a$  has the Rayleigh distribution:

$$p(a) = \frac{a}{\sigma^2} e^{-\frac{a^2}{2\sigma^2}}, \quad (6)$$

where  $\sigma$  is the standard deviation of the real and imaginary part of the cross correlation function and  $n$  is the total number

of spectrum points. In the case when all points of the spectrum are *statistically independent*, the cumulative distribution function of the coherent sum over  $n$  points is (Thompson et al. 2001)

$$P(a) = \left( 1 - e^{-\left(\frac{a^2}{2\sigma^2}\right)} \right)^n. \quad (7)$$

Differentiating this expression, we find the probability density function of the ratio of the amplitude of the coherent sum of spectrum samples of the noise to its standard deviation as

$$p(a) = n \frac{a}{\sigma^2} e^{-\frac{a^2}{2\sigma^2}} \left( 1 - e^{-\frac{a^2}{2\sigma^2}} \right)^{n-1}. \quad (8)$$

Under an assumption that all samples are *statistically independent*, the variance of the noise of the coherent sum of  $N$  samples is scaled as  $\sigma = \sigma_s / \sqrt{t_s S_r}$ , where  $S_r$  is the sampling rate of the recorded signal ( $6.4 \cdot 10^7$  in our experiment),  $t_s$  is the scan duration, and is  $\sigma_s$  the variance of an individual sample, 1 for a perfect system.

However, the assumption of statistical independence is an idealization. The presence of systematic phase errors, deviation of the bandpass from the rectangular shape and other factors distort the distribution. The deviation from the statistical independence is difficult to assess analytically.

We evaluate the variance of the noise by estimating the variance over a sample of 32768 random points at the region of the Fourier transform of the coherent sum of the cross-correlation that does not contain the signal. The indexes of grid elements of the sample are produced by using the random number generator. The sample of amplitudes is ordered, and one half of the points greater than the median is rejected. The variance over remaining points is computed and an iterative procedure is launched that adds back previously rejected points in the ascending order of their amplitudes and it updates the mean value and variance. The iterations are run till the maximum amplitude of the next sample reaches  $3.5\sigma_a$ . The initial rejection and consecutive restoration of points with amplitudes  $> 3.5\sigma_a$  ensures that no points with the signal from the source affect computation of  $\sigma_a$  and  $\langle a \rangle$ . The rejection of the tail of the amplitude distribution causes a bias in estimate of the mean, but the magnitude of the bias is only  $\sim 2 \cdot 10^{-4}$ , which is negligible. We define a signal to noise ratio as  $\text{SNR} = a/\langle a \rangle$ . It follows immediately from expression 6 that  $\langle a \rangle = \sqrt{\frac{\pi}{2}} \sigma$ .

We assume that the a posteriori distribution of the signal to noise ratios  $s = a/\sigma_a$  can be approximated as a function like expression 8 with effective parameters  $\sigma_{\text{eff}}$  and  $n_{\text{eff}}$ :

$$p(s) = \frac{2}{\pi} \frac{n_{\text{eff}}}{\sigma_{\text{eff}}} s e^{-\frac{s^2}{\pi}} \left( 1 - e^{-\frac{s^2}{\pi}} \right)^{n_{\text{eff}}-1}. \quad (9)$$

These parameters  $\sigma_{\text{eff}}$  and  $n_{\text{eff}}$  can be found by fitting the left tail of the empirical distribution of the signal to noise ratios. Using their estimates, we can evaluate the probability of finding the amplitude less than  $a$  if no signal is present, i.e. the probability of false detection:

$$P_f(s) = 1 - \int_0^s p(s) ds = 1 - \frac{1}{\sigma_{\text{eff}}} \left( 1 - e^{-\frac{s^2}{\pi}} \right)^{n_{\text{eff}}}. \quad (10)$$

The low end portion of the empirical SNR distribution and



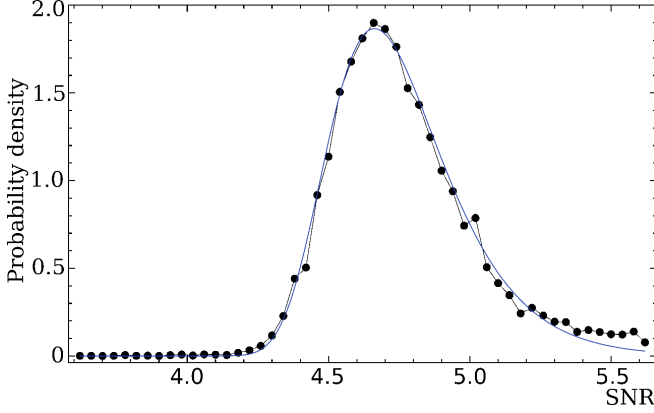


**Figure 1.** The low end of the empirical distribution of the achieved SNR for the fringe amplitude from results of fringe fitting VLBA data (filled circles) and the fitted curve (thin line) of the theoretical distribution for the case of no signal.

the table of the probability of false detection for VGaPS experiments are shown in Figure 1 and Table 4.

**Table 4**  
The probability of false detection as a function of SNR

| SNR  | $P_f(s)$  |
|------|-----------|
| 4.96 | 0.3       |
| 5.19 | 0.1       |
| 5.61 | 0.01      |
| 5.99 | 0.001     |
| 6.68 | $10^{-5}$ |

#### 3.2.4. Fine fringe search

Finally, the group delay, phase delay rate, group delay rate and fringe phase at the reference frequency are estimated using LSQ in the vicinity of the maximum provided its amplitude exceeds the detection limit. The goal of the LSQ refinement is to get realistic estimates of statistical errors of fitted parameters and to account for possible systematic errors by analyzing residuals. All cross-correlation spectrum data points of a given observation are used in a single LSQ solution with weights reciprocal to their variance.

Determining the variance of the fringe phase of an individual point is trivial only in two extreme cases: when  $\text{SNR} \ll 1$ , and when  $\text{SNR} \gg 1$ . In the first case the fringe phase distribution becomes uniform in the range of  $[0, 2\pi]$  with the variance  $\pi/\sqrt{3} \approx 1.813$ . In the second case expanding the expression for fringe phase in the presence of noise  $\phi = \arctan \frac{S_i + n_i}{S_r + n_r}$ , where  $S_i$  and  $S_r$  are the real and imaginary parts of the signal and  $n_i$  and  $n_r$  are the real and imaginary parts of the noise, into the Taylor series, neglecting terms  $O(n/S^2)$ , and evaluating the variance of the expansion, we get  $\sigma_\phi = \sqrt{\frac{2}{\pi}} \frac{1}{\text{SNR}}$ . For the general case, the problem becomes more difficult, since the  $\sigma_\phi$  depends on the variance of the noise and on the amplitude of the signal non-linearly. An analytical solution requires evaluation of complicated integrals that are not expressed via elementary functions.

We used the Monte Carlo approach for computing these variances. Let us consider a random complex set  $s = A + n_r + in_i$ , where  $A$  is the amplitude of the simulated signal and  $n_r, n_i$  are independent random variables with Gaussian dis-

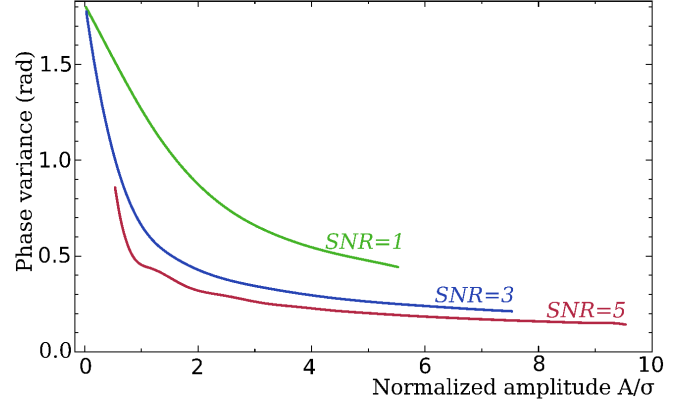


**Figure 2.** The variance of fringe phase as a function of the normalized amplitude  $A/\sigma_n$  in the presence of a signal with given SNR.

tribution. Their variance  $\sigma$  was selected in such a way that  $A = \sqrt{\frac{\pi}{2}} \sigma \text{SNR}$ . Then for a given SNR, we can compute the variance of phase of  $s$  as a function of the normalized amplitude  $|s|/\sigma$ . This is done by generation a long series (1 billion points) of the simulated complex signal for a given SNR, computing the amplitude and phase of the time series, splitting the signal into a uniform grid of 128 bins over normalized amplitude that spans the interval  $[\text{SNR} - 4.5, \text{SNR} + 4.5]$ , computing the variance of the phase of the simulated signal over all points that fall into each bin, and approximating the dependence of  $\sigma_\phi(|s|/\sigma)$  with a smoothing B-spline of the 3rd order over 6 nodes. We computed  $\sigma_\phi(|s|/\sigma)$  for SNRs in the range  $[0, 12.7]$  with steps of 0.1. Examples of this dependence for several SNRs are shown in figure 2. The set of B-spline coefficients forms a two dimensional table with axes SNR and normalized amplitude that allows evaluating  $\sigma_\phi$  for a given SNR and a given fringe amplitude.

It should be noted that the SNR of the coarse search is related to the amplitude coherently averaged over *all* valid cross-correlation spectrum samples,  $\sum_k^{N_t} \sum_j^{N_s} w_{kj}$ , where  $N_t$  is the number of accumulation periods and  $N_s$  is the total number of spectral channels. The SNR of *an individual* accumulation period (the elementary SNR) is  $\sqrt{\sum_k^{N_t} \sum_j^{N_s} w_{kj}}$  times less. For our experiments, the typical reduction of the SNR is a factor of 340. This means that for almost all sources the elementary SNR will be less than 1. As we have seen previously, the distribution of fringe phases at very low SNR's is close to uniform with a variance of  $\pi/\sqrt{3}$ . The phase becomes uncertain due to the  $2\pi$  ambiguity, and the LSQ estimation technique loses its diagnostic power. Therefore, the cross-correlation function with applied phase, phase delay rate and group delays computed during the coarse fringe search have to be coherently averaged over time and frequency in segments large enough to have sufficiently high SNR over a segment to provide an ambiguous phase. As it is seen in Figure 3, the fringe phase distribution at  $\text{SNR}=1$  is already sharp enough for that. Therefore, the number of spectral channels and the number of accumulation periods within a segment is chosen in such a way that the SNR be at least 1. Marginally detected scans with  $\text{SNR}=5$  have 24 segments that average all spectral channels within an IF and over 1/3 of the scan interval.

Using all segments, we determine four fitting parameters  $\mathbf{p}$  using the LSQ:

$$\mathbf{p} = (\mathbf{A}^\top \mathbf{W} \mathbf{A})^{-1} \mathbf{A}^\top \mathbf{W} \phi_s, \quad (11)$$

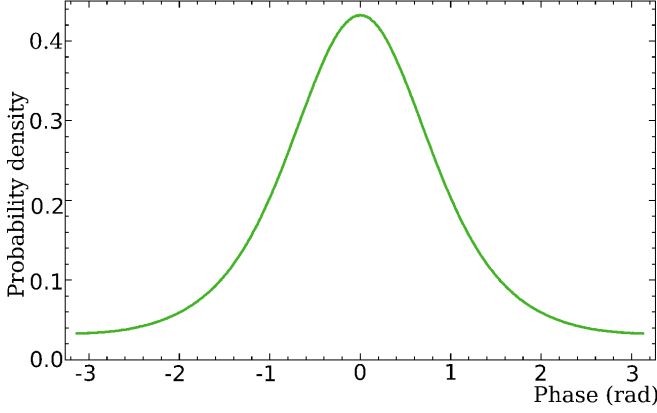


Figure 3. The probability density distribution of fringe phase with SNR=1.

where  $A$  is the matrix of observations,  $\mathcal{W}$  is the diagonal weight matrix and  $\phi_s$  is the vector phases of the cross-correlation function averaged over segments.

The mathematical expectation of the square of the weighted sum of residuals  $R$  in the presence of noise  $\epsilon$  is

$$E(R) = \text{Tr}(\mathcal{W}\text{Cov}\epsilon) - \text{Tr}(\text{Cov}\epsilon \mathcal{W} A (A^T \mathcal{W} A)^{-1} A^T \mathcal{W}), \quad (12)$$

which is reduced to  $n-m$  where  $n$  is the number of equations and  $m$  is the number of estimated parameters if the weight matrix  $\mathcal{W}$  is chosen to be  $(\text{Cov}\epsilon)^{-1}$ .

The presence of additive errors, for example fluctuations in the atmosphere, will increase  $\text{Cov}\epsilon$  and our estimate of the error variance based on the amplitude of the spectrum sample without knowledge of the scatter of the cross-spectrum phases is incomplete. A small additive noise with the variance  $k$  times less than the amplitude of the signal affects the amplitude as  $O(k^2)$ , but it affects phase as  $O(k)$ . One of the measures of the incompleteness of the error model is the ratio of the square of the weighted sum of residuals to its mathematical expectation.

We can extend our error model assuming that the weight matrix is  $\mathcal{W} = \text{Cov}\epsilon^{-1} - q^2 I$ , where  $I$  is the unit matrix of the same dimensions as  $\mathcal{W}$  and  $q$  is the parameter. This model is equivalent to an assumption that the used squares of weight of each segment were less than the true one by some parameter  $q$  equal to all segments. The mathematical expectation of  $R$  for this additive weighting model is

$$E(R) = n - m + q^2 [\text{Tr}(\mathcal{W}) - \text{Tr}(\mathcal{W} A (A^T \mathcal{W} A)^{-1} A^T)]. \quad (13)$$

Inverting 13, we find  $q$  for a given  $E(R)$ :

$$q = \sqrt{\frac{E(R) - (n - m)}{\text{Tr}(\mathcal{W}) - \text{Tr}(\mathcal{W} A (A^T \mathcal{W} A)^{-1} A^T)}}. \quad (14)$$

Replacing the mathematical expectation of  $R$  with its value evaluated from the residuals, we can find the re-weighting parameter  $q$  for a given solution. Several iterations provides a quick convergence of  $\frac{E(R)}{R}$  to 1. Applying an additive reweighting constant results in an increase in estimates of parameter uncertainties. It may happen that  $q$  becomes imaginary. This means that  $\mathcal{W}$  was overestimated. In our analysis we set  $q = 0$  in that happens.

### 3.2.5. Complex bandpass calibration

Coherent averaging of the cross-correlation spectrum over frequencies assumes that the data acquisition system does not introduce a distortion of the recorded signal, but this is usually not the case. Each intermediate frequency has its own arbitrary phase offset and group delay that may vary with time. The imperfection of baseband filters results in a non-rectangular shape of the amplitude response.

For calibrating these effects, a rail of narrow-band phase calibrator signals with spacing of 1 MHz was injected near the receivers. Two tones per IF are extracted by the data acquisition hardware, and their phase and amplitude are available for data analysis. When the phase of the phase calibration signal is subtracted from fringe phases, the result is referred to the point of injection of the phase calibration signal and this procedure is supposed to take into account any phase changes that occurred in the signal passing through the data acquisition terminal. However, we should be aware of several complications that emerge when we try to use the benefits of the phase calibration signal. First, the phases of two tones of the phase calibration signal separated by 6 MHz, as in our sessions, have ambiguities. Since the instrumental group delay may reach several phase turns over a 8 MHz IF, the second phase calibration tone is useless without resolving the ambiguity. Second, the phase calibration itself may have a phase offset or may become unstable if its amplitude is not carefully tuned. Therefore, we need to re-calibrate the phase calibration signal itself in order to successfully apply it to data.

We compute the complex bandpass function for each station, except the reference station, that describes the residual instrumental complex bandpass after applying the phase calibration signal. The cross-correlation spectrum needs to be divided by the complex bandpass in order to correct the instrumental frequency-dependent delay and fading of the amplitude. The procedure for evaluating the complex bandpass has several steps.

First, all data are processed applying the first tone of the phase calibration, i.e. the phase of the phase calibration signal is subtracted from each phase of the cross-correlation signal at a given IF.

Second, the bandpass reference station is chosen. Then for each station, we find an observation at a baseline with the reference station that provided the maximum SNR during the first run. Then for each IF we average the residual spectrum over time and perform a linear fit to the residual phases for determination of the instrumental group delay. Using this instrumental group delay, we extrapolate the phase of the phase calibration signal of the first phase calibration tone to the frequency of the second phase calibration tone and resolve its phase ambiguity. After that, we re-run the fringe search procedure for these scans by applying the phase calibration phase to each IF in the form of a linear function of phase versus frequency that is computed from two phase calibration tones with resolved phase ambiguity. The result of the new fringe search gives a new residual spectrum. Then we averaged the residual spectrum, over time and over  $M$  segments within each IF ( $M = 2$  in our experiment). The amplitude of the spectrum is normalized by dividing the average amplitude over all IFs. The phase and the amplitude of the residual averaged spectrum are approximated with a Legendre polynomial of degree 5. The result of this approximation as a complex function of frequency defines the so-called initial complex bandpass. Analysis of residuals of rejected observations helps to diagnose malfunction of the equipment. For example, one or more video-converters may fail, which may result in a loss of co-



herence. In that case, the part of the affected cross-correlation spectrum is masked out.

Third, we refine the complex bandpass. We select  $N$  more observations with the highest SNR from the first run at all baselines ( $N=16$  in our experiment) and re-run the fringe fitting procedure with applied phase (but not amplitude!) of the initial bandpass. We compute a residual spectrum averaged over time and  $M$  segments for each processed observation and normalize its amplitude. Then we fit a set of 6 coefficients of the Legendre polynomial for each station, except the reference one, for each IF, for both amplitude and phase to the phase and amplitude of the residual spectrum using a single LSQ solution. Then the residuals are computed and the observations with the maximum absolute value of residual phases and residual amplitudes are found separately. If the maximum absolute value of residual phase or residual amplitude exceeds the predefined limit, the affecting observation is removed and the solution is repeated. Iterations are run until either the absolute values of all remaining residuals are less than the predefined limit or the number of observations at a given baseline drops below  $N/2$ . The fitted Legendre polynomial coefficients are added to the coefficients of the initial bandpass and the result defines the so-called fine complex bandpass.

Fourth, all observations are reprocessed with the fine bandpass applied: the phase of the fine complex bandpass of the remote station of a baseline is subtracted and the phase of the bandpass of the reference station of a baseline is added before fringe fitting, and the amplitude is divided by the square root of the products of bandpass amplitudes after fringe fitting. Examples of residual phases before and after calibration are shown in figure 4.

### 3.3. Computation of total group delays and phase delay rates

The results of the fringe search are residual phase and group delay as well as their time derivatives determined from analysis of an observation at a given baseline of a given scan with respect to the a priori delay model used by the correlator. We need to compute the total path delay related to a certain moment of time common to all observations of a scan, called a scan reference time ( $t_{\text{srt}}$ ).

For logistical reasons, fringe searching at different baselines is performed independently and therefore, each observation has its own reference epoch, called a fringe reference times ( $t_{\text{frr}}$ ). This time epoch is computed as the weighted mean epoch of a given observation. Since stations usually start and end at slightly different time and the number of processed samples may be different, in general,  $t_{\text{frr}}$  is different at different baselines of the same scan. The scan duration may be significantly different at different stations either by a schedule design when antennas with different sensitivities participate in observations — this is often made in geodetic observations, or due to losses of some of the observing time at stations for various reasons. If we set  $t_{\text{srt}}$  as an average of  $t_{\text{frr}}$  over all baselines of a scan, it may happen that for some baselines the difference  $t_{\text{srt}} - t_{\text{frr}}$  may reach several hundred seconds. Setting a common  $t_{\text{srt}}$  for as many baselines as possible is desirable since it allows computation of delay triangle misclosures and some other important statistics. On the other hand, the uncertainty of the group delay estimate is minimal at  $t_{\text{frr}}$ . The uncertainty in group delay at  $t_{\text{srt}}$  grows as

$$\sigma_{\tau}^2(t_{\text{srt}}) = \sigma_{\tau}^2(t_{\text{frr}}) + 2 \text{Cov}(\tau, \dot{\tau})(t_{\text{srt}} - t_{\text{frr}}) + \sigma_{\dot{\tau}}^2(t_{\text{srt}} - t_{\text{frr}})^2, \quad (15)$$

which is undesirable. In our work, we set the tolerance limit for the growth of the the uncertainty due to the differences between  $t_{\text{srt}}$  and  $t_{\text{frr}}$ :  $0.1\sigma$  or 5 ps, whichever is less. Setting this limit, we find for each observation the maximum allowed  $|t_{\text{srt}} - t_{\text{frr}}|$  by solving quadratic equation 15. In the case where all observations of a scan have overlapping intervals of acceptable scan reference times, we set it to the value that minimizes  $2 \sum \text{Cov}(\tau, \dot{\tau})(t_{\text{srt}} - t_{\text{frr}}) + \sigma_{\dot{\tau}}^2(t_{\text{srt}} - t_{\text{frr}})^2$  over all observations. In the case where there are observations that have intervals of acceptable  $t_{\text{srt}}$  which are not overlapping, the set of observations of a scan is split into several subsets with overlapping acceptable  $t_{\text{srt}}$  and the optimization procedure is performed under each subset. Finally,  $t_{\text{srt}}$  is rounded to the nearest integer second.

The VLBA correlator shifts the time tag of data streams from each station to the moment of time when the wavefront reaches the center of the coordinate system. This operation facilitates correlation and allows station-based processing. The a priori path delay is computed for this modified time tag. This shift of the time tag depends on the a priori parameters of the geometric models, and therefore the total path delay produced from such a modified quantity would depend on errors of the a priori model which would considerably complicate data analysis. Therefore, we have to undo this shift of the time tag for the reference station of a baseline for further processing.

The correlator delay model for the VLBA hardware and software correlators is computed as a sum of a 5th degree polynomial fit to the geometric delays, the linear clock offset, and the coarse atmospheric model delay over intervals of 120 s length. We find the a priori delay of the baseline reference station  $\tau_a^{\text{rf}}$  related to the time tag at TAI of the wavefront arrival to its phase center from the implicit equation

$$\tau_a^{\text{rf}} = \sum_{k=0}^{k=5} a_i^{\text{rf}} (t_{\text{srt}} - t_o - (\tau_a^{\text{rf}} - \tau_{\text{cl}}^{\text{rf}} - \dot{\tau}_{\text{cl}}^{\text{rf}} \tau_a^{\text{rf}} - \tau_{\text{atm}}^{\text{rf}}))^k, \quad (16)$$

which is solved by iterations. Here  $t_o$  is the TAI time tag of the polynomial start time,  $\tau_{\text{cl}}^{\text{rf}}$  and  $\tau_{\text{atm}}^{\text{rf}}$  are the clock model and the atmosphere contribution of the a priori path model. We set  $\tau_a^{\text{rf}}$  on the right hand side of expression 16 to zero for the first iteration. Three iterations are sufficient to reach the accuracy 0.1 ps. Using the value  $\tau_a^{\text{rf}}$  found at the last iteration, we compute the a priori path delay for the remote station of the baseline:

$$\tau_a^{\text{rm}} = \sum_{k=0}^{k=5} a_i^{\text{rm}} (t_{\text{srt}} - t_o - (\tau_a^{\text{rf}} - \tau_{\text{cl}}^{\text{rm}} - \dot{\tau}_{\text{cl}}^{\text{rm}} \tau_a^{\text{rf}} - \tau_{\text{atm}}^{\text{rm}}))^k. \quad (17)$$

The a priori delay rate is computed using an expression similar to equation 17. Finally, we compute the total path delay by extrapolating the residual delay to the scan reference time:

$$\tau_{\text{tot}} = \tau_{\text{apr}}^{\text{rm}} - \tau_{\text{apr}}^{\text{rf}} + \tau_{\text{res}} + \dot{\tau}_{\text{res}}(t_{\text{srt}} - t_{\text{frr}}). \quad (18)$$

The delay produced this way is the difference between the interval of proper time measured by the clock of the remote station between events of arrival of the wave front to the reference point of the remote antenna and clock synchronization in TAI and the interval of proper time measured by the clock of the reference station between events of arrival of the wave front to the reference point of the reference antenna and clock synchronization in TAI.

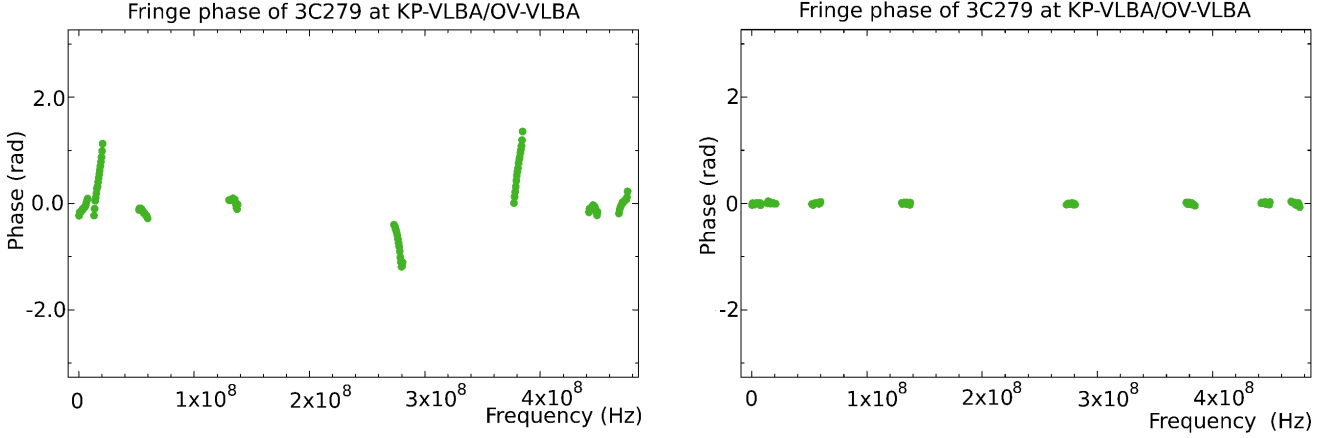


**Figure 4.** Residual fringe phases (radians) before (left) and after (right) applying bandpass calibration in experiment bp125b.

### 3.4. Astrometric Analysis: Delay Modeling

Our computation of theoretical time delays in general follows the approach presented in detail by Sovers et al. (1998) with some refinements. The most significant ones are the following. The advanced expression for time delay derived by Kopeikin and Schäfer (1999) in the framework of general relativity was used. The displacements caused by the Earth's tides were computed using the numerical values of the generalized Love numbers presented by Mathews (2001) following a rigorous algorithm described at Petrov and Ma (2003) with truncation at a level of 0.05 mm. The displacements caused by ocean loading were computed by convolving the Greens' functions with ocean tide models using the NLOADF algorithm of Agnew (1997). The GOT00 model Ray (1999) of diurnal and semi-diurnal ocean tides, the NAO99 model of ocean zonal tides (Matsumoto et al. 2000), the equilibrium model (Petrov and Ma 2003) of the pole tide, and the tide with period of 18.6 years were used. Atmospheric pressure loading was computed by convolving the Greens' functions with the output of the atmosphere NCEP Reanalysis numerical model (Kalnay et al. 1996). The algorithm of computations is described in full details in Petrov and Boy (2004). The empirical model of harmonic variations in the Earth orientation parameters `heo_20091201`<sup>5</sup> derived from VLBI observations according to the method proposed by Petrov (2007a) was used. The time series of UT1 and polar motion from the Goddard operational VLBI solutions were used as a priori.

The a priori path delays in the neutral atmosphere in directions towards observed sources were computed by numerical integration of differential equations of wave propagation through the heterogeneous media. The four-dimensional field of the refractivity index distribution was computed using the atmospheric pressure, air temperature and specific humidity taken from the output of the Modern Era Retrospective-Analysis for Research and Applications (MERRA) (Schubert et al. 2008). That model presents the atmospheric parameters at a grid  $1/2^\circ \times 2/3^\circ \times 6^h$  at 72 pressure levels.

For considering the contribution of the ionosphere to the phase of the cross-correlation spectrum, notice that the elec-

tromagnetic wave propagates in a plasma with phase velocity

$$v_p = \frac{c}{\sqrt{1 - \frac{N_v e^2}{m_e \epsilon_o \omega^2}}}, \quad (19)$$

where  $N_v$  — electron density,  $e$  — charge of an electron,  $m_e$  — mass of an electron,  $\epsilon_o$  — permittivity of free space,  $\omega$  — angular frequency of the wave and  $c$  — velocity of light in vacuum. Phase velocity in the ionosphere is faster than the velocity of light in vacuum.

After integration along the ray path and expanding expression 19, withholding only the term of the first order, we get the following expression for additional phase rotation caused by the ionosphere:

$$\Delta\phi = -\frac{a}{\omega}, \quad (20)$$

where  $\omega$  is the angular frequency and  $a$  is

$$a = \frac{e^2}{2c m_e \epsilon_o} \left( \int N_v ds_1 - \int N_v ds_2 \right). \quad (21)$$

Here  $s_1$  and  $s_2$  are the paths of wave propagation from the source to the first and second station of the baseline. If  $\int N_v ds$  is expressed in units of  $1 \cdot 10^{16}$  electrons/m<sup>2</sup> (so-called TEC units), then after having substituted values of constants, we get  $a = 5.308018 \cdot 10^{10} \text{ sec}^{-1}$  times the difference in the TEC values at the two stations.

Since the ionosphere contribution is frequency-dependent, it distorts the fringe-fitting result. Taking into account that the bandwidth of the recorded signal is small with respect to the observed frequency, we can linearize eqn. 20 near the reference frequency  $\omega_o$ :  $\phi = -a/\omega_o + a(\omega_i - \omega)/\omega_o^2$ . Comparing it with expression 4, we see that the first frequency-independent term contributes to the phase delay and the second term, linear with frequency, contributes to the group delay. The fine fringe search is equivalent to solving the LSQ for  $\tau_p$  and  $\tau_g$  using the following system of equations:

$$\tau_p \omega_o + \tau_g (\omega_k - \omega_o) = \phi_i + \frac{a}{\omega_i}, \quad (22)$$

where index  $i$  runs over frequencies and index  $k$  runs over accumulation periods.

<sup>5</sup> Available at <http://astrogeo.org/erm>

A solution of the  $2 \times 2$  system of normal equations that originates from equations 22 can be easily obtained analytically. Gathering terms proportional to  $a$ , we express the contribution of the ionosphere to phase and group delay as  $\tau_p^{\text{iono}} = -a/\omega_p^2$  and  $\tau_g^{\text{iono}} = a/\omega_g^2$ , where  $\omega_p$  and  $\omega_g$  are effective ionospheric frequencies:

$$\omega_p = \sqrt{\frac{\sum_i^n w_i \cdot \sum_i^n w_i (\omega_i - \omega_o)^2 - \left( \sum_i^n w_i (\omega_i - \omega_o) \right)^2}{\sum_i^n w_i (\omega_i - \omega_o) \sum_i^n w_i \frac{(\omega_i - \omega_o)}{\omega_i} - \sum_i^n w_i (\omega_i - \omega_o)^2 \cdot \sum_i^n \frac{w_i}{\omega_i}}} \quad (23)$$

$$\omega_g = \sqrt{\frac{\sum_i^n w_i \cdot \sum_i^n w_i (\omega_i - \omega_o)^2 - \left( \sum_i^n w_i (\omega_i - \omega_o) \right)^2}{\sum_i^n w_i (\omega_i - \omega_o)^2 \sum_i^n \frac{w_i}{\omega_i} - \sum_i^n w_i \cdot \sum_i^n w_i \frac{(\omega_i - \omega_o)}{\omega_i}}}$$

where  $w_i$  is the weight assigned to the fringe phase at the  $i$ th frequency channel.

They have a clear physical meaning: if the wide-band signal was replaced by a quasi-monochromatic signal with a group or phase effective ionosphere frequency, then the contribution to group or phase delay of the wide-band signal would be the same as the contribution of the quasi-monochromatic signal at those effective frequencies.

For computing the contribution of the ionosphere, we used the total electron contents (TEC) maps from analysis of linear combinations of GPS observables made at two frequencies, 1.2276 and 1.57542 GHz. Using GPS-derived TEC maps for data reduction of astronomic observations, first suggested by Ros (2000), has become a traditional approach for data processing. Analysis of continuous GPS observations from a global network comprising 100–300 stations makes it feasible to derive an empirical model of the total electron contents over the span of observations using the data assimilation technique. Such a model is routinely delivered by GPS data analysis centers since 1998. For our analysis we used the TEC model provided by the GPS analysis center CODE (Schaer 1998). The model gives values of the TEC in zenith direction on a regular 3D grid with resolutions  $5^\circ \times 5^\circ \times 2^h$ .

For the purpose of modeling, the ionosphere is considered as a thin spherical layer with constant height  $H$  above the Earth's surface. The typical value of  $H$  is 450 km. In order to compute the TEC from GPS maps, we need to know the coordinates of the point at which the ray pierces the ionosphere — point  $J$  in figure 5. First, we find the distance from the station to the ionosphere piercing point  $D = |AJ|$  by solving triangle  $OAJ$ . Noticing that  $|OA| = R_\oplus$  and  $|OJ| = R_\oplus + H$ , we immediately get

$$\beta = \arcsin \frac{\cos E}{1 + \frac{H}{R_\oplus}} \quad (24)$$

$$D = R_\oplus \sqrt{2 \frac{H}{R_\oplus} (1 - \sin(E + \beta)) + \left( \frac{H}{R_\oplus} \right)^2},$$

where  $E$  is the elevation of the source above the horizon.

Then the Cartesian coordinates of point  $J$  are  $\vec{r} + D\vec{s}$ . Transforming them into polar coordinates, geocentric latitude and

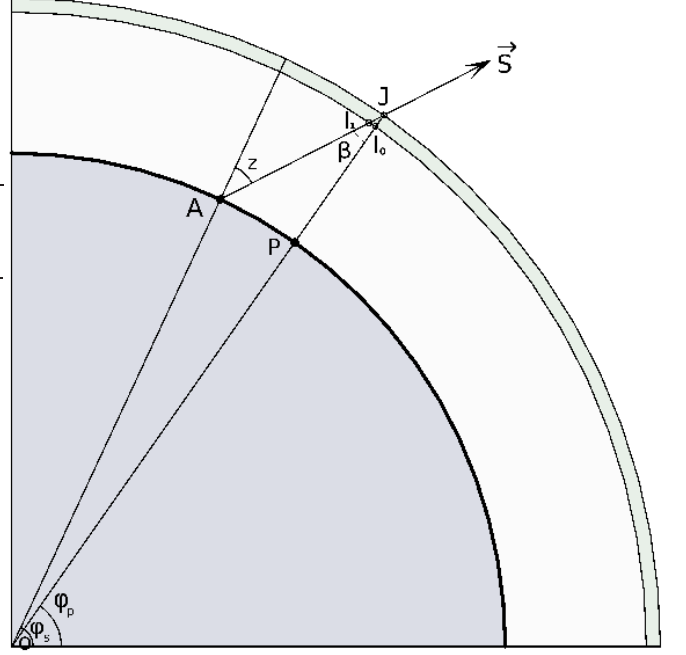


**Figure 5.** Ray traveling from the source  $\vec{s}$  to antenna  $A$  pierces the top of the ionosphere in the point  $J$  and the bottom of the ionosphere in the point  $I$ . The ionosphere is considered as a thin layer.  $P$  is the point on the Earth's surface beneath the ionosphere piercing point  $J$ .

longitude, we get arguments for interpolation in the 3D grid. We used the 3-dimensional B-spline interpolation by expanding the TEC field into the tensor products of basic splines of the 3rd degree. Interpolating the TEC model output, we get the TEC through the vertical path  $|JI_o|$ . The slanted path  $|JI_1|$  is  $|JI_o|/\cos \beta$ . Therefore, we need to multiply the vertical TEC by  $1/\cos \beta(E)$ , which maps the vertical path delay through the ionosphere into the slanted path delay. Here we neglect the ray path bending in the ionosphere. We also neglect Earth's ellipticity, since the Earth was considered spherical in the data assimilation procedure of the TEC model.

Combining equations, we get the final expression for the contribution of the ionosphere to path delay:

$$\tau_{\text{iono}} = \pm \frac{a}{4\pi^2 f_{\text{eff}}^2} \text{TEC} \frac{1}{\cos \beta(E)}, \quad (25)$$

where  $f_{\text{eff}}$  is the effective cyclic frequency, and the plus sign is for the group delay, and the minus sign is for the phase delay.

Computation of the theoretical path delay and its partial derivatives over model parameters is made with using software VTD<sup>6</sup>.

### 3.5. Astrometric Analysis: Parameter Estimation

Astrometric analysis is made in several steps. First, each individual 24 hour session is processed independently. The parameter estimation model includes estimation of 1) clock functions presented as a sum of a 2nd degree polynomial and a linear spline over 60 minutes; 2) residual zenith atmosphere path delay for each station presented as a linear spline; 3) coordinates of all stations, except a reference station; and 4) coordinates of the target sources. The goal of the coarse solution is to identify and suppress outliers. The main reasons for

<sup>6</sup> Available at <http://astrogeo.org/vtd>.



outliers are a) errors in determining the global maximum of the fringe amplitude during fringe search and b) false detections. Both errors decrease with increasing the SNR. Because of this, we initially run our solution by restricting to  $\text{SNR} \geq 6$ , and then restore good detections with SNR in the range of [5, 6].

After identifying outliers and removing them from our solution, we apply estimates of the parameters of the a posteriori model to outliers, which allows us to predict the path delay with accuracy better than 500 ps, except for sources that had fewer than two detections. Then we re-run the fringe search for outliers and restrict the search window to  $\pm 1000$  ps with respect to predicted delay. We also lower the SNR detection limit to 4.8, since the number of independent samples in the restricted search window, and therefore, the probability of false detection at a given SNR is less. This procedure allows to restore from 50 to 80% of observations marked as outliers in the previous step. The weights of observables were computed as  $w = 1/\sqrt{\sigma_o^2 + r^2(b)}$ , where  $\sigma_o$  is the formal uncertainty of group delay estimates and  $r(b)$  is the baseline-dependent reweighting parameter that was evaluated in a trial solution to make the ratio of the weighted sum of the squares of residuals to its mathematical expectation to be close to unity using the technique similar to that used for fine fringe search.

Finally, we run a global VLBI solution that uses all available observations to date, 7.56 million, from April 1980 through August 2010 in a single LSQ run. The estimated parameters are

- *global* (over the entire data set): coordinates of 4924 sources, including target objects in VGaPS campaign, positions and velocities of all stations, coefficients of B-spline expansion that model non-linear motion of 17 stations, coefficients of harmonic site position variations of 48 stations at four frequencies: annual, semi-annual, diurnal, semi-diurnal, and axis offsets for 67 stations.
- *local* (over each session): tilts of the local symmetric axis of the atmosphere (also known as “atmospheric azimuthal gradients”) for all stations and their rates, station-dependent clock functions modeled by second order polynomials, baseline-dependent clock offsets, and the Earth orientation parameters.
- *segmented* (over 20–60 minutes): coefficients of linear splines that model atmospheric path delays (20 minutes segment) and clock functions (60 minutes segment) for each station. The estimates of clock functions absorb uncalibrated instrumental delays in the data acquisition system.

The rate of change for the atmospheric path delays and clock functions between adjacent segments was constrained to zero with weights reciprocal to  $1.1 \cdot 10^{-14}$  and  $2 \cdot 10^{-14}$ , respectively, in order to stabilize solutions. We apply no-net rotation constraints on the positions of 212 sources marked as “defining” in the ICRF catalogue (Ma et al. 1998) that requires the positions of these source in the new catalogue to have no rotation with respect to the position in the ICRF catalogue to preserve continuity with previous solutions.

The global solution sets the orientation of the array with respect to an ensemble of  $\sim 5000$  extragalactic remote radio

sources. The orientation is defined by the series of Earth orientation parameters and parameters of the empirical model of site position variations over 30 years evaluated together with source coordinates. Common sources observed in VGaPS as atmosphere and amplitude calibrators provide a connection between the new catalogue and the old catalogue of compact sources.

### 3.6. Astrometric analysis: assessment of weights of observations

As follows from the Gauss-Markov theorem, the estimate of parameters has minimum dispersion when observation weights are chosen reciprocal to the variance of errors. The group delays used in the analysis have errors due to the thermal noise in fringe phases and due to mismodeling theoretical path delay in the atmosphere:

$$\sigma^2 = \sigma_{th}^2 + \sigma_{io}^2 + \sigma_{na}^2 \quad (26)$$

where  $\sigma_{th}^2$  is thermal noise,  $\sigma_{io}^2$  and  $\sigma_{na}^2$  are the contribution of the ionosphere and the neutral atmosphere to the error budget.

#### 3.6.1. A priori errors of the GPS ionosphere model

The first term,  $\sigma_{th}^2$ , was estimated during the fringe fitting. The second term can only be evaluated indirectly. Sekido et al. (2003) used six dual-band intercontinental VLBI sessions at 10 stations in July 2000 and compared TEC values from GPS with TEC estimated from VLBI observables. They drew a conclusion that the errors in path delay derived from the GPS TEC model were at the range of 70 ps at the zenith direction at 8.6 GHz. However, the ionosphere path delay is a non-stationary process. Therefore, great caution should be taken in an attempt to generalize conclusions made from analysis of a small network over a short time period. The non-stationarity of ionospheric fluctuations implies that there does not exist an exact expression for the variance of the ionosphere fluctuations during any given period, and any expression for the variance is an approximation.

Since June 1998 when the GPS TEC maps became available through August 2010, more than 2000 dual-band S/X VLBI sessions under geodesy and absolute astrometry programs were carried out, including 92 sessions at the VLBA. It can be easily shown that the contribution of the ionosphere at X-band,  $\tau_{xi}$  can be found from the linear combination of group delay observables with coefficients that are expressed through effective ionosphere frequencies at these bands  $\omega_x$  and  $\omega_s$  defined in expression 23:

$$\tau_{xi} = (\tau_x - \tau_s) \frac{\omega_s^2}{\omega_x^2 - \omega_s^2}. \quad (27)$$

We used this dataset for evaluation of the errors of the contribution of the ionosphere to group delays derived from GPS TEC maps, considering the ionosphere contribution from dual-band VLBI observations as true for the purpose of this comparison. We computed the ionosphere contribution from the GPS model and from VLBI observations for each session. The root mean squares (rms) of the differences of the contribution VLBI–GPS was computed for all sessions and all baselines. We sought regressors that can predict rms(VLBI–GPS). We expect the short-term variability of the ionosphere at scales less than several hours to dominate the errors of the GPS model. The sparseness of the GPS network and limited sky coverage result in missing high frequency spatial and temporal variations of the ionosphere. The turbulent nature of the

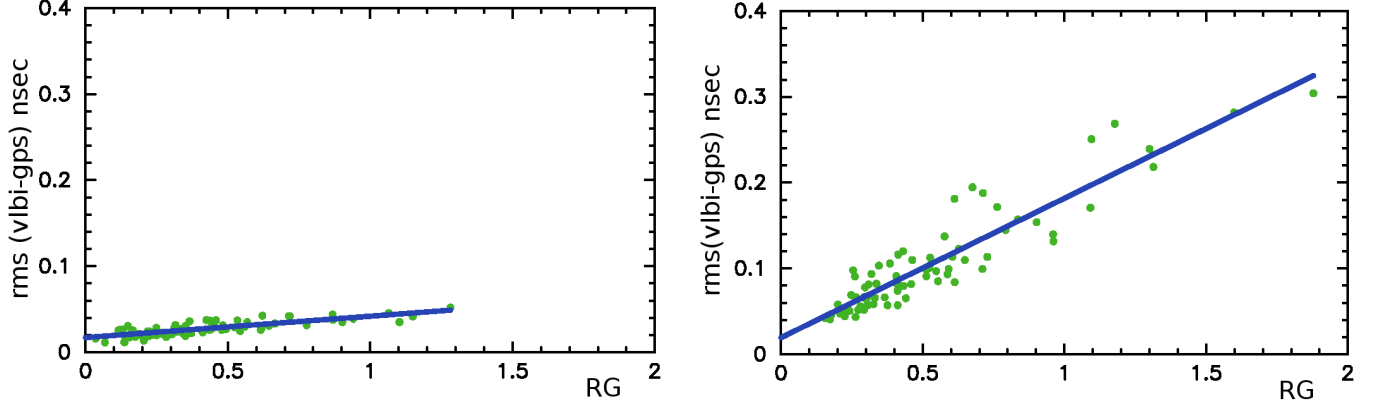


**Figure 6.** Dependence of the rms of the differences VLBI minus GPS as a function of  $RG = \sqrt{\text{rms}_{g1}^2 + \text{rms}_{g2}^2}$  for baseline FD-VLBA/PIETOWN, 565 km long (left) and for baseline LA-VLBA/MK-VLBA, 4970 km long (right). The quantity  $\text{rms}_{gi}$  is the rms of GPS path delay at the  $i$  station of a baseline during a session. Each green dot corresponds to one VLBI session. The thick blue straight light is a linear fit through the data.

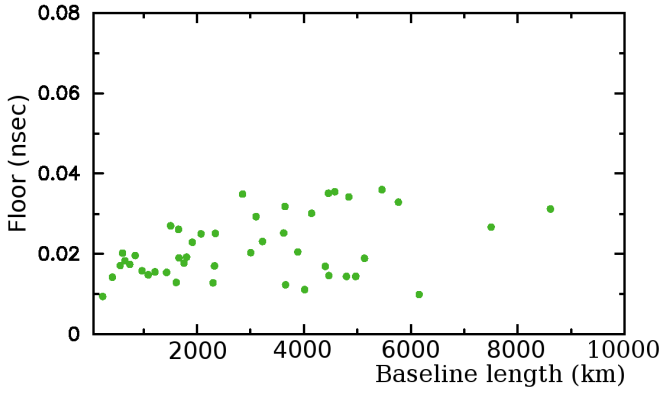


**Figure 7.** The floor of the regression model of the dependence of rms(VLBI-GPS) of  $RG = \sqrt{\text{rms}_{g1}^2 + \text{rms}_{g2}^2}$  for all VLBA baselines as a function of the baseline length.

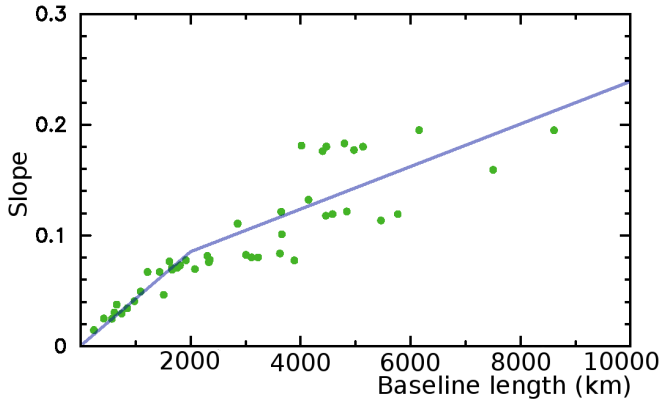


**Figure 8.** The slope of the regression model of dependence of rms(VLBI-GPS) of  $RG = \sqrt{\text{rms}_{g1}^2 + \text{rms}_{g2}^2}$  for all VLBA baselines as a function of the baseline length. The straight lines show a linear approximation of the slope for two ranges of the baseline length: below and over 2000 km.

ionosphere path delay variations suggests that the rms of the ionosphere model errors due to missed high frequency variations will be related to the rms of the low frequency variations either as a linear function or as a power law. After many tries we found that the following parameter can serve as a regressor:  $RG = \sqrt{\text{rms}_{g1}^2 + \text{rms}_{g2}^2}$ , where  $\text{rms}_{gi}$  is the rms of the GPS

path delay at the  $i$  th station of a baseline during a session. The  $\text{rms}_{g1}$  and  $\text{rms}_{g2}$  are highly correlated at short baselines and  $\sqrt{\text{rms}_{g1}^2 + \text{rms}_{g2}^2} > \text{rms}(g2 - g1)$ . At long baselines the ionosphere contribution de-correlates. Therefore, the dependence of rms(VLBI-GPS) versus RG will depend on the baseline length and possibly on other parameters. Figure 6 shows examples of this dependence for a short baseline and for a long baseline.

It is remarkable that rms(VLBI-GPS) versus RG fits reasonably well with a linear function. We computed rms(VLBI-GPS) for each baseline and fitted it to the linear model  $F + S \cdot RG$ . The floor of the linear fit has a mean value around 20 ps (Figure 7). As expected, the slope of the fit increases with baseline length as shown in Figure 8. The growth is linear up to baselines lengths of 2000 km, which apparently correspond to the decorrelation of the paths through the ionosphere. The growth of the slope beyond baseline lengths of 2000 km is slower and it shows more scatter.

We use this dependence for predicting the rms of the GPS ionosphere model errors. For each station that participated in the experiment we computed the rms of the ionosphere variations in zenith direction. Then we express the predicted variance of the GPS ionosphere model errors as

$$\sigma_i^2 = \left( F_b \frac{f_i^2}{f_{\text{eff}}^2} \right)^2 + \left( \tau_{\text{iono},1} - \frac{\bar{\tau}_1^z}{\cos \beta(E_1)} \right)^2 S_b^2 + \left( \tau_{\text{iono},2} - \frac{\bar{\tau}_2^z}{\cos \beta(E_2)} \right)^2 S_b^2, \quad (28)$$

where  $\tau_{\text{iono},i}$  is the ionosphere path delay at the  $i$  th station computed using the GPS TEC maps,  $\bar{\tau}_1^z$  the zenith ionosphere path delay from GPS TEC maps averaged over a 24<sup>h</sup> period with respect to the central date of the session,  $F_b$  and  $S_b$  are parameters of the linear model rms(VLBI-GPS) versus RG for a given baseline,  $f_i$  is the frequency for which the model was computed (8.6 GHz), and  $f_{\text{eff}}$  the frequency of the experiment for which the model is applied (24.5 GHz). The term  $\tau_{\text{iono},i} - \frac{\bar{\tau}_i^z}{\cos \beta(E_i)}$  is the difference between the ionosphere path delay from GPS at a given direction and the average ionosphere path delay scaled to take into account the elevation dependence. This term is an approximation of  $\text{rms}_{g1}$  used for computation of RG.

### 3.6.2. A priori errors of the path delay in the neutral atmosphere

Rigorous analysis of the errors of modeling the path delay in the neutral atmosphere is beyond the scope of this paper. Assuming the dominant errors of the a priori model are due to high frequency fluctuations of water vapor at scales less than 3–5 hours, we seek the regression model in the form of dependence of the rms of errors on the total path delay in the non-hydrostatic component of the path delay. We made several trial runs using all 123 observing sessions at the VLBA under geodesy and absolute astrometry programs with reciprocal weights modified according to

$$\sigma_{used}^2 = \sigma^2 + \left( a \cdot \frac{\tau_s}{\tau_z} \right)^2. \quad (29)$$

Here  $\tau_s$  is the contribution of the non-hydrostatic constituent of the slanted path delay and  $\tau_z$  is the non-hydrostatic path delay in the zenith direction computed by direct integration of the equations of wave propagation through the atmosphere using the refractivity computed from the MERRA model, and  $a$  is the coefficient. We found that when coefficient  $a = 0.02$  is used, the baseline length repeatability, defined as the rms of the deviation of baseline length with respect to the linear time evolution, reaches the minimum. We adopted value 0.02 in our analysis of VGaPS experiments. For typical values of  $\tau_z$ , the added noise is 8 ps in zenith direction and 80 ps at  $10^\circ$  elevation.

### 3.6.3. Ad hoc added variance of the noise

We also computed for each baseline and each session an ad hoc variance of observables that, added in quadrature, makes the ratio of the weighted sum of squares of post-fit residuals to their mathematical expectation close to unity in a similar way as we updated fringe phase weights. Expression 14 was used for computing this variance. This ad hoc variance was applied to further inflate the a priori observable uncertainties that have already been corrected for the inaccuracy of the a priori model of wave propagation through the ionosphere and the neutral atmosphere according to expressions 28 and 29. In contrast to 28 and 29, the baseline-dependent ad hoc variance is elevation independent.

## 4. VALIDATION OF THE WIDE-BAND FRINGE SEARCH ALGORITHM

Using *PLMA*, we detected 327 target sources versus 136 targets detected with AIPS, since the AIPS detection limit is lowered by a factor of  $\sqrt{8} = 2.83$ . Thus, the yield of the experiments was improved by the factor of 2.4 – a very significant improvement that well justified our efforts to create a new software package for processing astrometric observations.

Another difference is that the results of processing the data with AIPS have ambiguities in group delay that are reciprocal to the minimum difference between intermediate frequencies. This means that the group delays are  $\tau_g + K\tau_s$ , where  $\tau_s = 76.923$  ns and  $K$  is an arbitrary integer number. At the same time, the results of processing with the wide-band fringe fitting algorithm do not suffer this problem. The reason for group delay ambiguities is that the narrow-band fringe fitting algorithm implemented in AIPS first coherently averages the data within each IF, and in the second step of fringe fitting it processes a rail of narrow-band signals. The Fourier transform that describes the dependency of the amplitude of the coherent sum of the cross-spectrum on group delay has a periodicity that is reciprocal to the minimum frequency separation of IFs, 76.923 ns in our case. The wide-band fringe

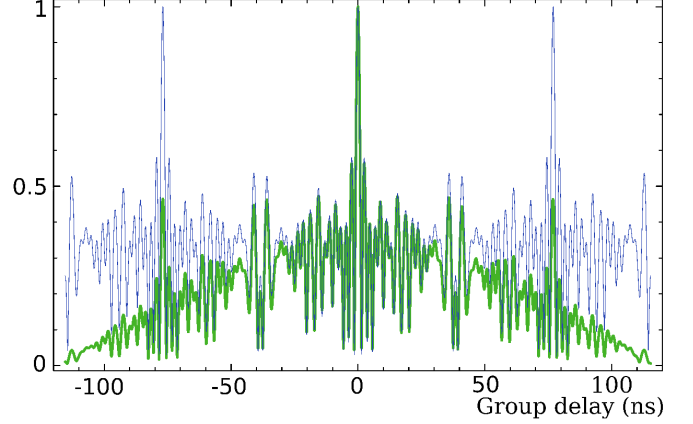


**Figure 9.** Coherent sum of cross-correlation amplitude, normalized to its value at the maximum as a function of group delay shift with respect to the maximum for VGaPS observing sessions. The thick green line shows result of processing with *PLMA*. The thin blue line shows results of processing with AIPS. The pattern of the thin blue line repeats with a period of 76.923 ns.

fitting algorithm does not average the spectrum. Therefore, the periodicity of the Fourier transform of the coherent sum of the cross-spectrum in the wide-band algorithm is equal to the spectral resolution, i.e. 2 mks for VGaPS experiments. Figure 9 illustrates this difference.

The lack of group delay ambiguities has a profound effect on determining source positions with poorly known a priori coordinates. In the presence of group delay ambiguities, we had to solve for source positions first using less precise so-called narrow-band group delays determined by arithmetic averaging group delays computed for each IF independently. The accuracy of these source position estimates is often insufficient to reliably resolve group delay ambiguities, especially in the presence of narrow-band group delay outliers. When the number of used observations is large, say more than 10, the data redundancy allows us to detect the presence of incorrectly resolved ambiguities and fix the problem. But if the number of observations is small, chances are the error in group delay ambiguity resolution will not be noticed. In the past, source position estimates made with less than 8 observations were considered unreliable. The use of the wide-band fringe fitting algorithm eliminates this problem entirely. Re-processing the old data revealed that group delay ambiguities for a considerable number of sources were indeed resolved incorrectly, which resulted in source position errors as large as 4"! In contrast, the wide-band fringe fitting algorithm provides reliable estimates of source positions using a minimum redundancy of 3 observations.

Since the wide-band fringe search algorithm is new, we would like to be sure that the new algorithm does not introduce new systematic errors with respect to the old one. As a validation test, we re-processed a set of 33 VLBA absolute astrometry/geodesy experiments under the RDV program (Petrov et al. 2009) and 12 VLBA absolute astrometry experiments under the K/Q program (Lanyi et al. 2010). Each test experiment had a duration of 24 hours.

The RDV experiments were observed on a global network, including all 10 VLBA stations, with dual-band receivers at 8.6 GHz (X band) and 2.3 GHz (S band), with 4 IFs allocated at X band and 4 IFs allocated at S band. Fringe fitting, outlier elimination, re-weighting, and in the case of AIPS, group delay ambiguity resolution, were made independently using



**Table 5**

Solution statistics from 33 global RDV sessions processed with AIPS and *PLIMA*. The statistics in the central column were computed using all observations. The statistics in the right column were computed using observations with SNR > 10.

|                                   | AIPS     | <i>PLIMA</i><br>SNR <sub>min</sub> = 5.0 | <i>PLIMA</i><br>SNR <sub>min</sub> = 10.0 |
|-----------------------------------|----------|------------------------------------------|-------------------------------------------|
| No. obs used                      | 467 769  | 531 299                                  | 472 717                                   |
| fit wrms                          | 18.40 ps | 21.22 ps                                 | 19.65 ps                                  |
| No. sources                       | 776      | 800                                      | 773                                       |
| wrms $\Delta\Psi \cos \epsilon_o$ | 0.10 mas | 0.12 mas                                 | 0.14 mas                                  |
| wrms $\Delta\epsilon$             | 0.10 mas | 0.10 mas                                 | 0.12 mas                                  |
| Bas. rep. at 5000 km              | 4.81 mm  | 4.75 mm                                  | 4.96 mm                                   |
| Bas. rep. at 9000 km              | 8.54 mm  | 8.08 mm                                  | 7.95 mm                                   |

*PLIMA* and AIPS. Subsequent data reduction and parameter estimation were made using identical setups. Estimated parameters of the solution were the same as in processing the VGaPS sessions, except for treatment of site positions: they were treated as local parameters, i.e. estimated for each session independently.

The statistics of the solution for 33 global RDV sessions using AIPS and *PLIMA* are shown in table 5. The weighted root mean squares (wrms) of the postfit residuals is larger in the *PLIMA* solution for two reasons. First, the *PLIMA* solution contain 14% more points, mainly with SNR's in the range [5.0, 10.0], that were undetected by the traditional AIPS algorithm. The errors of these observables are systematically larger. We rerun the *PLIMA* solution and excluded all points with SNR either at X- or S-band less than 10. The difference in wrms postfit residuals was significantly reduced. The second reason is that the group delay formal errors were inflated in *PLIMA* processing to make the ratio of postfit residuals of fringe fitting to its mathematical expectation close to 1. This was not done for the AIPS solutions.

Another test of goodness of the solution and possible presence of systematic errors is the so-called baseline length repeatability test (Petrov et al. 2009). We computed the wrms of baseline length estimates with respect to the fitted linear model of their evolution with time. The dependence of the baseline length wrms with the length of baselines  $L$  is fitted by function  $R(L) = \sqrt{A^2 + B^2 L}$ . Values of  $R(L)$  at  $L=5000$  km and  $L=9000$  km are presented in table 5. We also computed the wrms of the deviations of estimates of daily offsets of nutation angles in longitude,  $\Delta\psi$ , and nutation in obliquity,  $\Delta\epsilon$ , with respect to the empirical nutation expansion  $\text{heo\_20091201}$ . The statistics in table 5 show the satisfactory agreement between AIPS and *PLIMA* solutions and do not reveal any systematic differences.

Since the goal of VGaPS was to derive source positions, comparison of the positions from AIPS and *PLIMA* processing is important to evaluate the level of systematic differences. We, thus, computed the differences in sources coordinates  $\Delta\alpha \cos \delta(\alpha)$  and  $\Delta\delta(\delta)$ . We restricted our analysis to 528 sources that had more than 64 observations in both AIPS and *PLIMA* in order to avoid effects of a greater number of observations available in the *PLIMA* solutions. Plots of these differences are shown in figure 10 and position comparisons are shown in table 6. The table contains the results from 528 sources observed in RDV sessions with at least 64 used observations. The 2nd column shows statistics of differences between AIPS and *PLIMA* with an SNR cutoff of 5. The 3rd column shows the differences between AIPS and *PLIMA* so-

**Table 6**

Differences between AIPS and *PLIMA* positions of 528 sources observed in RDV experiments. The differences in the left column were computed using all observations. The differences in the right column were computed using observations with SNR > 10.

|                                         | AIPS- <i>PLIMA</i><br>SNR <sub>min</sub> = 5.0 | AIPS- <i>PLIMA</i><br>SNR <sub>min</sub> = 10.0 |
|-----------------------------------------|------------------------------------------------|-------------------------------------------------|
| wrms $\Delta\alpha \cos \delta(\alpha)$ | 0.072 mas                                      | 0.020 mas                                       |
| wrms $\Delta\delta(\delta)$             | 0.088 mas                                      | 0.032 mas                                       |

lutions with an SNR cutoff of 10. These differences are only about 20% of a typical position uncertainty.

In the right plot of Figure 10 we can see a small systematic declination differences at low declinations. Similar differences but produced from *PLIMA* solution made with the SNR cutoff 10.0, shown in Figure 11, help to understand the origin of this pattern. When the SNR cutoff is raised to 10, the wrms of differences are reduced by 2–3 times to 0.02–0.03 mas and the systematic pattern disappear. For comparison, the average formal uncertainties for declinations are 0.12 mas and for right ascensions scaled by  $\cos \delta$  are 0.07 mas, so the systematic errors are small. Sources at low declinations observed on a VLBI array located in the northern hemisphere are necessarily taken at low elevations. Including in a solution additional low SNR observations at low elevations, unavailable in the AIPS solutions, changes the contribution of systematic errors due to mismodeling path delay in the neutral atmosphere that are higher at low elevations. At present, it is not clear whether including observations with SNR in range 5–10 increases systematic errors, or the opposite, including these observations reduces the systematic errors. However, the magnitude of the differences, less than 0.5 mas as declinations in the range  $[-50^\circ, -25^\circ]$  does not raise a concern.

Finally, we have re-analyzed 12 VLBA experiments under the K/Q program. The frequency setup in K/Q and VGaPS campaigns was identical. Lowering the detection limit by a factor of  $\sqrt{8} \approx 2.83$  with the use of the wide-field fringe fitting algorithm greatly helped. Processing the data with *PLIMA* did not detect only 8 out of the 340 observed sources, with 61 non-detections in data processing with AIPS. We compiled table 7 of statistics of the K/Q solution in a form similar to table 5. Analysis of source position differences did not reveal any pattern of systematic errors. The statistics of these differences presented in table 8 do not exceed formal uncertainties of positions which are 0.08 mas and 0.14 mas in right ascensions scaled by  $\cos \delta$  and declination, respectively. The first column is four sources with an SNR cutoff of 5, the second column with an SNR cutoff of  $5 \cdot \sqrt{8} = 14.1$ . The baseline length repeatability and the wrms of nutation offset time series from *PLIMA* solutions are 20–30% smaller. We do not have an explanation why *PLIMA* solution produces noticeably better results for 24 GHz observations, but no significant improvement was found from analysis of S/X RDV experiments.

The above results of analysis of validation runs processing 0.6 million observations at K, X and S bands, collected during 1080 hours of recording at the VLBA and the global VLBI network with both AIPS and *PLIMA* demonstrate that the new wide-band algorithm for group delays does not introduce any significant systematic errors while detecting more sources because it evaluates group delays using the coherent sum of the data across the wide-band. We conclude that *PLIMA* has passed major validation tests.

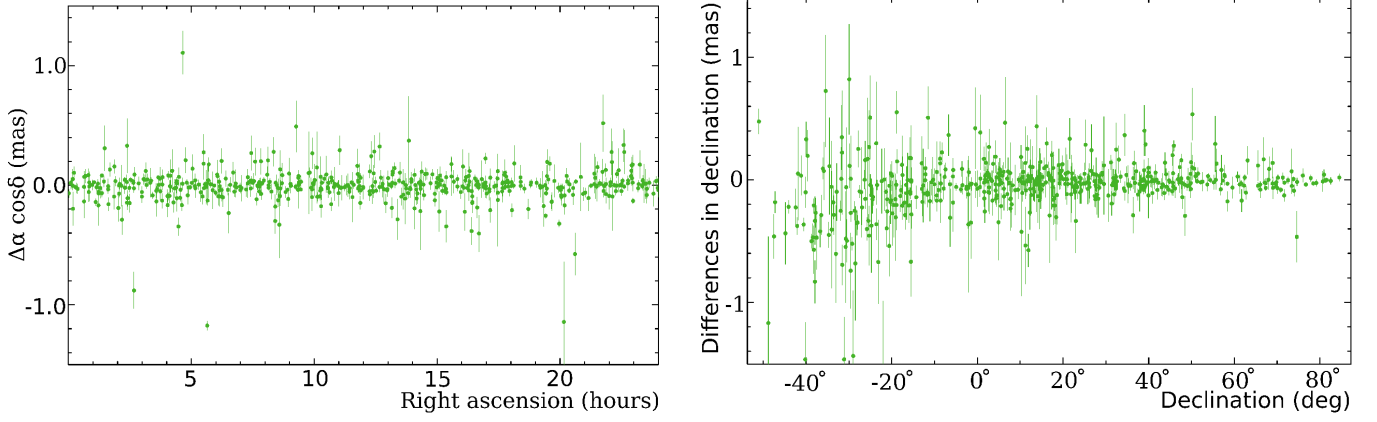


**Figure 10.** Systematic differences in source coordinate estimates between solutions using group delays derived by *PLMA* and by AIPS. Left plot shows  $\Delta\alpha \cos \delta$  ( $\alpha$ ), right plots shows  $\Delta\delta$  ( $\delta$ ).

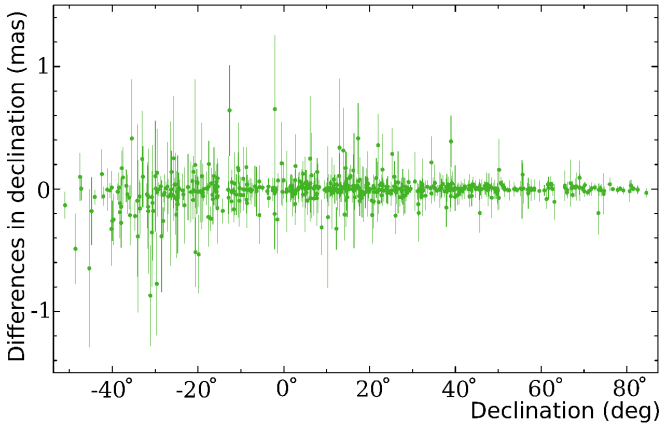


**Figure 11.** Systematic differences  $\Delta\delta(\delta)$  in source coordinate estimates between solutions using group delays derived by *PLMA* with SNR cutoff 10 and by AIPS.

**Table 7**

Solution statistics from 12 VLBA experiments at 24 GHz under the K/Q program processed with AIPS and *PLMA*. The statistics in the central column were computed using all observations. The statistics in the right column were computed using observations with SNR > 10.

|                                   | AIPS     | <i>PLMA</i><br>SNR <sub>min</sub> = 5.0 | <i>PLMA</i><br>SNR <sub>min</sub> = 14.1 |
|-----------------------------------|----------|-----------------------------------------|------------------------------------------|
| # Obs used                        | 104 887  | 139 213                                 | 105 761                                  |
| fit wrms                          | 19.50 ps | 23.08 ps                                | 19.19 ps                                 |
| # Sources                         | 279      | 332                                     | 276                                      |
| wrms $\Delta\Psi \cos \epsilon_o$ | 0.13 mas | 0.10 mas                                | 0.09 mas                                 |
| wrms $\Delta\epsilon$             | 0.18 mas | 0.13 mas                                | 0.14 mas                                 |
| Bas. rep. at 5000 km              | 5.56 mm  | 4.58 mm                                 | 4.58 mm                                  |
| Bas. rep. at 9000 km              | 9.29 mm  | 7.36 mm                                 | 7.32 mm                                  |

**Table 8**

Differences between AIPS and *PLMA* positions of 244 sources observed in the K/Q VLBA experiments. The differences in the left column were computed using all observations. The differences in the right column were computed using observations with SNR > 10.

|                                         | AIPS- <i>PLMA</i><br>SNR <sub>min</sub> = 5.0 | AIPS- <i>PLMA</i><br>SNR <sub>min</sub> = 10.0 |
|-----------------------------------------|-----------------------------------------------|------------------------------------------------|
| wrms $\Delta\alpha \cos \delta(\alpha)$ | 0.062 mas                                     | 0.060 mas                                      |
| wrms $\Delta\delta(\delta)$             | 0.108 mas                                     | 0.096 mas                                      |

## 5. INVESTIGATION OF SYSTEMATIC ERRORS IN SOURCE POSITIONS

Using single-band data, ionosphere path delay mismodeling may produce systematic position errors. Lanyi et al. (2010) showed that in their analysis of K-band observations systematic errors reached several mas and had a tendency to be larger at low declinations. In section 3.6.1 we evaluated the rms of random errors caused by ionosphere path delay mismodeling. However, inflating weights to account for the variance of errors in general does not guarantee that source positions will have no systematic errors.

To evaluate the magnitude of possible ionosphere driven systematic errors we made the following Monte Carlo simulation. We added to the theoretical path delay the zero-mean Gaussian noise  $M \cdot N(0, \sigma_i)$ , with the variance  $\sigma_i$  computed according to expression 28. The noise was magnified  $M$  times in order to make the contribution of ionosphere path delay errors dominant over other sources of errors. We made 64 analysis runs of VGaPS data using different seeds of the random noise generator. The magnification factor 100 was used. Thus, we produced 64 estimates of position of each source with added noise. We computed the rms of position estimates of each target source and divided it by  $M$ . To the extent of the validity of expression 28, these rms's represent expected errors due to the inadequacy of the ionosphere path delay models based on using the TEC models derived from GPS analysis. Plots of  $\Delta\alpha_i(\delta)$  and  $\Delta\delta_i(\delta)$  errors are shown in Figures 12–13. For 90% of the sources, errors are at the level of 0.02–0.04 mas.  $\Delta\delta(\delta)$  increases to 0.1 mas at declinations less than  $-20^\circ$ , and for some sources may reach 0.4 mas. The disparity in systematic errors for sources at comparable declinations reflects the disparity in the number of observables used in the solution.

For assessment of remaining systematic errors we exploited that fact that 56 known sources were observed as amplitude and atmospheric calibrators. Positions of these sources are known from previous dual-band S/X observations with accuracies better than 0.1 mas. We split the set of 56 calibrators into two subsets of 28 objects and ran two additional solutions. In the first solution we suppressed 28 calibrators in all sessions except VGaPS and determined their positions solely from VGaPS. In the second solution we did the same with the second subset. Considering that the positions of calibrators from numerous S/X observations can be regarded as true for the purpose of this comparison, we treated the differences as VGaPS errors.

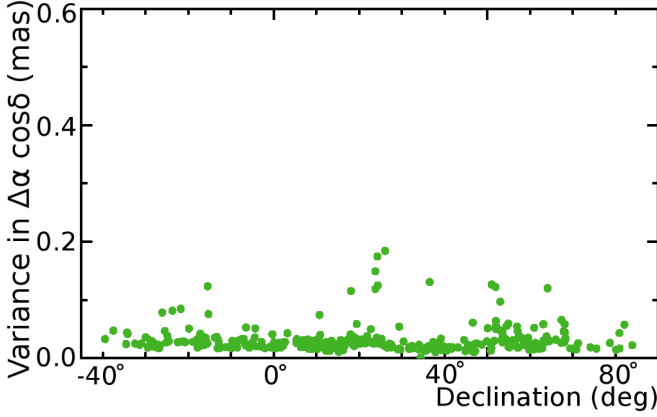


**Figure 12.** Modeled systematic errors  $\Delta\alpha_i(\delta)\cos\delta$  driven by the mismodeling ionosphere path delay contribution evaluated from the Monte Carlo simulation.

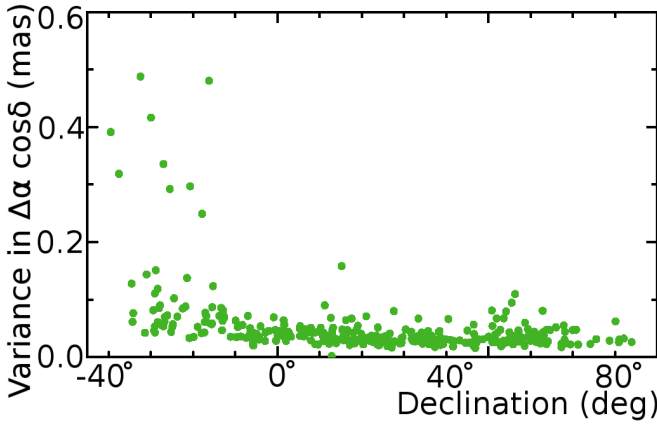


**Figure 13.** Modeled systematic errors  $\Delta\delta^i(\delta)$  driven by the mismodeling ionosphere path delay contribution evaluated from the Monte Carlo simulation.

We computed the  $\chi^2$  per degree of freedom statistics for the differences in right ascensions and declinations  $\Delta\alpha$  and  $\Delta\delta$  and sought additional variances  $v_\alpha$  and  $v_\delta$  that, being added in quadrature to the source position uncertainties, will make them close to unity:

$$\frac{\chi_\alpha^2}{\text{ndf}} = \frac{\sum_{k=1}^{k=n} \Delta\alpha_k^2 \cos^2 \delta_k}{n \sum_{k=1}^{k=n} \sqrt{\sigma_{\alpha,k}^2 \cos^2 \delta_k + \alpha_{i,k}^2 + v_\alpha^2 \cos^2 \delta_k}} \quad (30)$$

$$\frac{\chi_\delta^2}{\text{ndf}} = \frac{\sum_{k=1}^{k=n} \Delta\delta_k^2}{n \sum_{k=1}^{k=n} \sqrt{\sigma_{\delta,k}^2 + \delta_{i,k}^2 + v_\delta^2}}$$

The denominator in equation 30 is a mathematical expectation of the sum of squares of differences, provided the estimates of source positions are statistically independent.

We found the following additive corrections of the uncertainties in right ascensions scaled by  $\cos\delta$  and for declinations respectively:  $v_\alpha = 0.08$  mas and  $v_\delta = 0.120$  mas.

The final inflated errors of source positions,  $\sigma_\alpha^2(f)$  and

$\sigma_\delta^2(f)$ , are

$$\begin{aligned} \sigma_\alpha^2(f) &= \sigma_\alpha^2 + v_\alpha^2 + \alpha_i^2 / \cos^2 \delta \\ \sigma_\delta^2(f) &= \sigma_\delta^2 + v_\delta^2 + \delta_i^2 \end{aligned} \quad (31)$$

Position of some sources may indeed be different due to the core-shift effect (Kovalev et al. 2008, Porcas 2009). Treatment of this shift as VGaPS errors makes our estimates of reweighting parameters and therefore reported final inflated errors somewhat too conservative.

## 6. IMAGING

For imaging purposes we performed the a priori calibration of the data following a traditional way, using AIPS (Greisen 1988). In the future, we plan to introduce all extra steps required for an accurate amplitude calibration into *PLMA* as well.

We followed the usual AIPS initial VLBA calibration procedure involving a priori amplitude calibration with measured antenna gain curves and system temperatures as well as sampling-based calibration adjustments. Atmospheric absorption is significant at 24 GHz. We have estimated its effect using system temperature data covering the whole range of elevations and weather information in order to adjust visibility amplitudes for the opacity. Typical values of the opacity were found to range between 0.03 and 0.1 for different VLBA telescopes and observing epochs. We performed phase calibration using the phase calibration signal injected during observations and fringe fitting. A separate solution for station-based group delay and phase delay rate was made for each frequency channel (IF). As the final step of calibration, band-pass corrections were determined and applied.

Our observations were scheduled around 24 GHz since the K-band continuum performance is better at this frequency, away from the water line. Unfortunately, at the time of these observations most of the VLBA telescopes had no gain curve measurements close to 24 GHz. It has changed since 2007 when regular 24 GHz gain curve measurements started to be performed at all VLBA stations. For all VLBA antennas but MK-VLBA and HN-VLBA we have used gain curves measured at 22.2 GHz while for the former the curves at 23.8 GHz were applied. Antenna efficiency as well as the noise diode spectrum do change with frequency (see, e.g., Petrov et al. 2007c, as well as results of VLBA gain curve measurements at 22 and 24 GHz after 2007<sup>7</sup>). This is one of the main sources of the total amplitude calibration uncertainty. Additionally, IFs in our experiment are widely spread (Table 2) which might introduce extra amplitude shifts. We used strong flat-spectrum sources in the sample in order to estimate global relative amplitude correction factors for different IFs but did not find any to be larger than 10% with high confidence. No extra frequency channel specific amplitude corrections were applied to the data.

After a priori calibration, data were imported to the Caltech DIFMAP package (Shepherd 1997), visibility data flagged, and images were produced using an automated hybrid imaging procedure originally suggested by Greg Taylor (Pearson et al. 1994) which we optimized for our experiment. The procedure performs iterations of phase and amplitude self-calibration followed by CLEAN image reconstruction. We were able to reach the VLBA image thermal noise level for most of our final CLEAN images. Examples of 3

<sup>7</sup> [http://www.vlba.nrao.edu/astro/VOBS/astronomy/vlba\\_gains.ke](http://www.vlba.nrao.edu/astro/VOBS/astronomy/vlba_gains.ke)



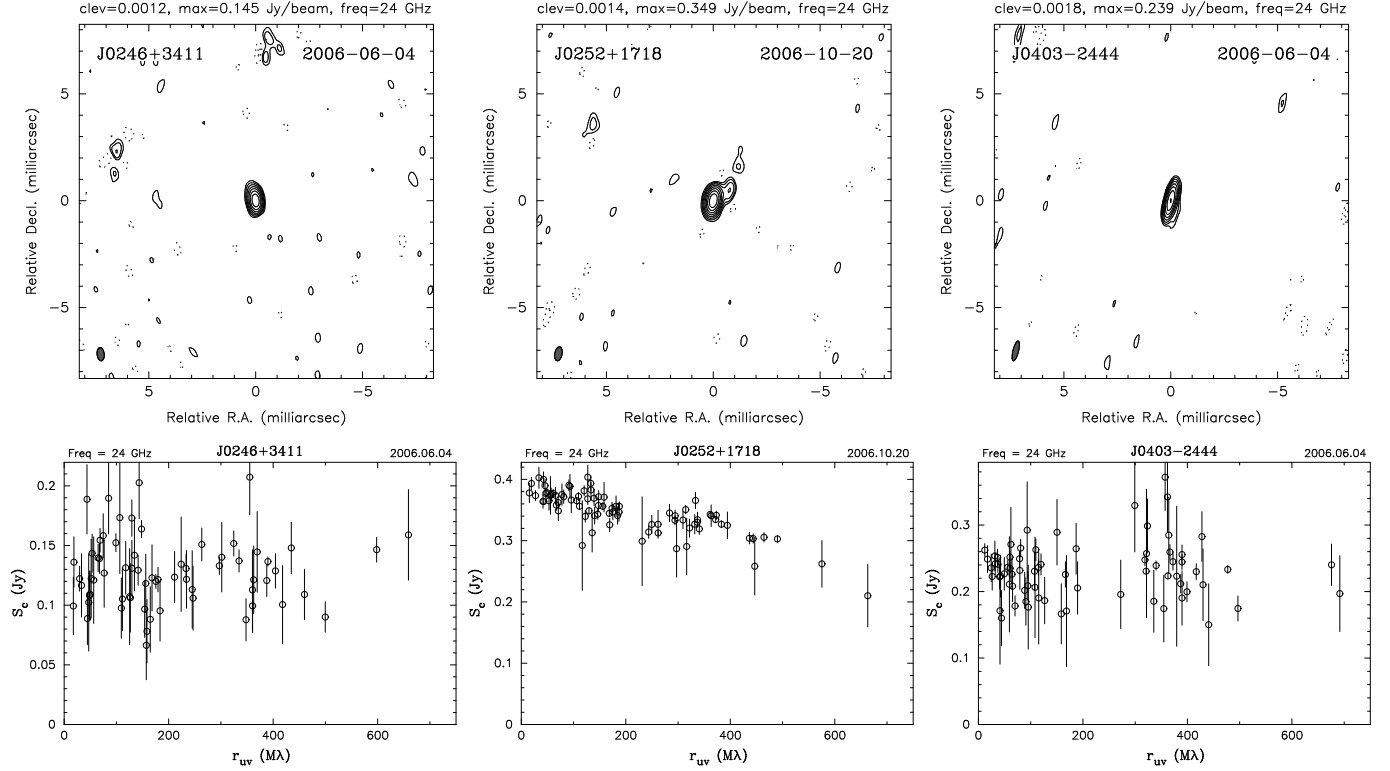


**Figure 14.** From top to bottom. *Row 1:* Naturally weighted CLEAN images at 24 GHz. The lowest contour is plotted at the level given by “clev” in each panel title (Jy/beam), the peak brightness is given by “max” (Jy/beam). The contour levels increase by factors of two. The dashed contours indicate negative flux. The beam is shown in the bottom left corner of the images. *Row 2:* Dependence of the correlated flux density on projected spacing. Each point represents a coherent average over one 2 min observation on an individual interferometer baseline. The error bars represent only the statistical errors.

images, for compact and resolved objects, are shown in Figure 14.

Total errors of our measurements of correlated flux density values for sources stronger than  $\sim 200$  mJy were dominated by the accuracy of amplitude calibration described above. This considers the error of amplitude calibration as not exceeding 15% and this estimate is confirmed by our comparison of the flux densities integrated over the VLBA images with the single-dish flux densities which we measured with RATAN-600 in 2006 for slowly varying sources without extended structure. Details of the RATAN-600 single-dish observing program including the method of observations and data processing can be found in Kovalev et al. (1999, 2002).

## 7. THE CATALOGUE OF SOURCE POSITIONS

Of 487 sources observed, three or more detections were found for 327 objects. After careful identification and removal of outliers due to the incorrect selection of the global maximum for weak sources with  $\text{SNR} < 6$ , we selected 33,452 observations out of 59,690 from three VGaPS experiments for analyzing in the single LSQ solution together with 7.56 million other VLBI observations. The semi-major error ellipses of inflated position errors for all sources except 0903+154 vary in the range 0.21 to 20 mas with the median value of 0.85 mas. The histogram of position errors is shown in Figure 15.

The VGaPS catalogue is listed in Table 9. Although positions of all 5047 astrometric sources were adjusted in the LSQ solution that included the VGaPS sources, only coordinates of 327 target sources observed in the VGaPS campaign are pre-

sented in the table. The first column gives calibrator class: “C” if the source is recommended as a calibrator or “U” if it has an unreliable position, since there were less than 5 detections and there is a risk that the secondary maximum of the coherent sum of weighted complex cross-correlation samples has been picked and has not been flagged out. The second and third columns give the IVS source name (B1950 notation) and IAU name (J2000 notation). The fourth and fifth columns give source coordinates at the J2000.0 epoch. Columns /6/ and /7/ give source position uncertainties in right ascension and decli-

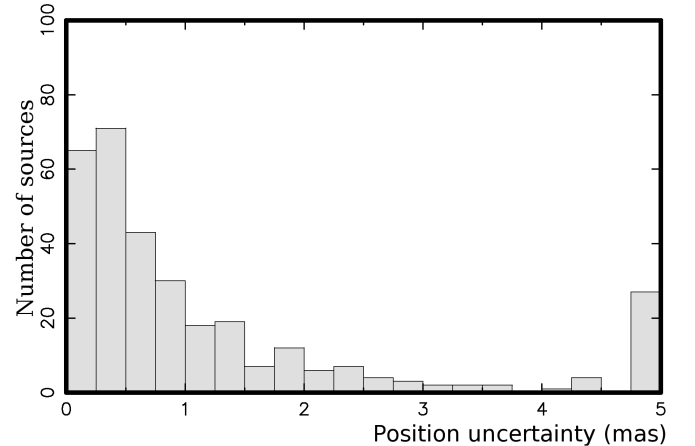


**Figure 15.** The histogram of the semi-major axes of inflated position error ellipses among 327 target sources in the VGaPS catalogue. The last bin shows errors exceeding 4.75 mas.

**Table 9**  
The VGaPS catalogue

| Source name |          |            | J2000.0 Coordinates |                 | Errors (mas) |                |                | Correlated flux density (in Jy) |       |        |       |
|-------------|----------|------------|---------------------|-----------------|--------------|----------------|----------------|---------------------------------|-------|--------|-------|
| Class       | IVS      | IAU        | Right               | ascension       | Declination  | $\Delta\alpha$ | $\Delta\delta$ | Corr                            | # Obs | Total  | Unres |
| (1)         | (2)      | (3)        | (4)                 | (5)             | (6)          | (7)            | (8)            | (9)                             | (10)  | (11)   |       |
| C           | 2358+605 | J0001+6051 | 00 01 07.099852     | +60 51 22.79800 | 0.94         | 0.51           | -0.115         | 123                             | 0.11  | 0.11   |       |
| C           | 2359+606 | J0002+6058 | 00 02 06.696680     | +60 58 29.83950 | 4.42         | 1.92           | -0.168         | 26                              | 0.09  | < 0.08 |       |
| C           | 0002+541 | J0005+5428 | 00 05 04.363368     | +54 28 24.92414 | 0.60         | 0.47           | 0.167          | 79                              | 0.34  | 0.11   |       |
| C           | 0003+505 | J0006+5050 | 00 06 08.249784     | +50 50 04.41150 | 0.68         | 0.81           | -0.041         | 64                              | 0.16  | 0.14   |       |
| C           | 0005+568 | J0007+5706 | 00 07 48.468649     | +57 06 10.43705 | 1.81         | 2.18           | 0.631          | 46                              | 0.08  | 0.09   |       |
| C           | 0012+610 | J0014+6117 | 00 14 48.792125     | +61 17 43.54198 | 0.57         | 0.29           | -0.034         | 153                             | 0.25  | 0.16   |       |
| C           | 0024+597 | J0027+5958 | 00 27 03.286191     | +59 58 52.95899 | 0.56         | 0.34           | -0.214         | 136                             | 0.23  | 0.16   |       |
| C           | 0032+612 | J0035+6130 | 00 35 25.310605     | +61 30 30.76122 | 0.94         | 0.52           | -0.038         | 117                             | 0.13  | 0.10   |       |
| C           | 0034-220 | J0037-2145 | 00 37 14.825799     | -21 45 24.71171 | 1.17         | 2.78           | -0.834         | 59                              | 0.09  | 0.09   |       |
| C           | 0039+568 | J0042+5708 | 00 42 19.451680     | +57 08 36.58569 | 0.39         | 0.25           | 0.046          | 162                             | 0.48  | 0.32   |       |
| C           | 0041+677 | J0044+6803 | 00 44 50.759596     | +68 03 02.68540 | 0.67         | 0.29           | -0.163         | 154                             | 0.23  | 0.19   |       |
| C           | 0044+566 | J0047+5657 | 00 47 00.428864     | +56 57 42.39373 | 0.53         | 0.39           | 0.006          | 154                             | 0.18  | 0.13   |       |

**Note.** — Table 9 is presented in its entirety in the electronic edition of the Astronomical Journal. A portion is shown here for guidance regarding its form and contents. Units of right ascension are hours, minutes and seconds. Units of declination are degrees, minutes and seconds.

nation in mas after applying inflated errors according to equation 31 (without  $\cos \delta$  factor), and column /8/ gives the correlation coefficient between the errors in right ascension and declination. The number of group delays used for position determination is listed in column /9/. Column /10/ gives the estimate of the flux density integrated over the entire map. This estimate is computed as a sum of all CLEAN components if a CLEAN image was produced. If we did not have enough detections of the visibility function to produce a reliable image, the integrated flux density is estimated as the median of the correlated flux density measured at projected spacings less than 70 M $\lambda$ . The integrated flux density is the source total flux density with spatial frequencies less than 12 M $\lambda$  filtered out, or in other words, the flux density from all details of a source with size less than 20 mas. Column /11/ gives the flux density of unresolved components estimated as the median of correlated flux density values measured at projected spacings greater than 400 M $\lambda$ . For some sources no estimates of the unresolved flux density are presented, because either no data were collected at the baselines used in calculations, or these data were unreliable.

The on-line version of this catalogue is posted on the Web<sup>8</sup>. For each source it has 4 references: to a FITS file with CLEAN components of naturally weighted source images; to a FITS file with calibrated visibility data; to a postscript map of a source; and to a plot of correlated flux density as a function of the length of the baseline projection to the source plane.

In Table 10 we present a priori coordinates, total flux densities extrapolated to 24 GHz and spectral index estimates for 160 target objects that have not been detected in the VGaPS experiment. Some of these sources were detected in other VLBI astrometry experiments at S/X bands.

## 8. COMPARISON OF K- AND X/S-BAND ASTROMETRIC VLBI POSITIONS

We searched the VLBI archive and found that among our target sources, 206 were observed with S/X at the VLBA under VCS and RDV programs before November 2010. We investigated the differences in K-band observations against independent S/X observations. We restricted our analysis to 192 objects that had uncertainties from X/S and K band solutions

<sup>8</sup> <http://astrogeo.org/vgaps>

**Table 10**

The list of 160 sources that have not been detected in VGaPS observations.

| Source names | Right ascens. | Declination  | gal. lat.    | Flux  | Sp.Ind. | #        |
|--------------|---------------|--------------|--------------|-------|---------|----------|
| (1)          | (2)           | (3)          | (4)          | (5)   | (6)     | (7) (8)  |
|              |               | h m s        | ° ' "        | deg   | mJy     |          |
| 2359+548     | J0002+5510    | 00 02 00.470 | +55 10 38.00 | -6.8  | 121.    | -0.03 2  |
| 0003+669     | J0006+6714    | 00 06 10.000 | +67 14 38.30 | 5.0   | ...     | ... 0    |
| 0009+655     | J0012+6551    | 00 12 37.671 | +65 51 10.82 | 3.5   | 195.    | -0.59 8  |
| 0010+722     | J0013+7231    | 00 12 58.750 | +72 31 12.76 | 10.1  | 501.    | 0.02 8   |
| 0017+590     | J0020+5917    | 00 20 24.550 | +59 17 30.50 | -3.1  | 324.    | -0.02 6  |
| 0018-194     | J0021-1910    | 00 21 09.370 | -19 10 21.30 | -79.6 | ...     | ... 0    |
| 0028+592     | J0031+5929    | 00 31 03.120 | +59 29 45.30 | -3.0  | 3855.   | 1.52 2   |
| 0041+660     | J0044+6618    | 00 44 41.300 | +66 18 42.00 | 3.7   | 119.    | -0.91 7  |
| 0107+562     | J0110+5632    | 01 10 57.553 | +56 32 16.93 | -5.9  | 267.    | -0.66 10 |
| 0113+241     | J0116+2422    | 01 16 38.067 | +24 22 53.72 | -37.8 | 168.    | -0.03 7  |
| 0128+554     | J0131+5545    | 01 31 13.860 | +55 45 13.20 | -6.4  | 150.    | -0.06 5  |

**Note.** — Table 10 is presented in its entirety in the electronic edition of the Astronomical Journal. A portion is shown here for guidance regarding its form and contents. Columns 1–2 show IAU B1950 and J2000 source names, columns 3–5 show a priori source positions at the J2000.0 epoch, column 6 shows extrapolated a priori total flux density at 24 GHz, column 7 shows coarse estimate of the spectral index, and column 8 shows the number of measurements of flux density found in the CATS database that were used for evaluation of the flux spectral index and extrapolation the flux density.

less than 5 mas. Figures 16 show the differences in right ascensions and declinations.

### 8.1. Special cases: 3C 119 and 3C 410

Positions of two sources, J0432+4138 (also known as 3C119) and J2020+2942 (3C410) are found to be significantly off, namely 38.3 and 38.0 mas respectively. The significance of this offset, 55 and 72 times of inflated uncertainties, is too high to be explained by known error sources. RATAN-600 observations have shown that both of them continuously show steep radio spectra and are slowly variable. On VLBI scales, they were found to have significantly extended structure (e.g., Figures 17,18).

One of these compact steep spectrum radio sources, the object J0432+4138, is well studied at parsec scales. Recent high-dynamic range images at 5 and 8.4 GHz and full bibliography on historic observations can be found in Mantovanni et al. (2010). This source shows several bright components at 24 GHz. Two of them, namely components ‘A’ and ‘C’ (Figure 17), are located 40.6 mas apart. The feature C is stronger, its total flux density is 0.54 Jy, but more extended. The FWHM of a circular Gaussian component fitted to the feature is found to be 1.4 mas. The feature A is

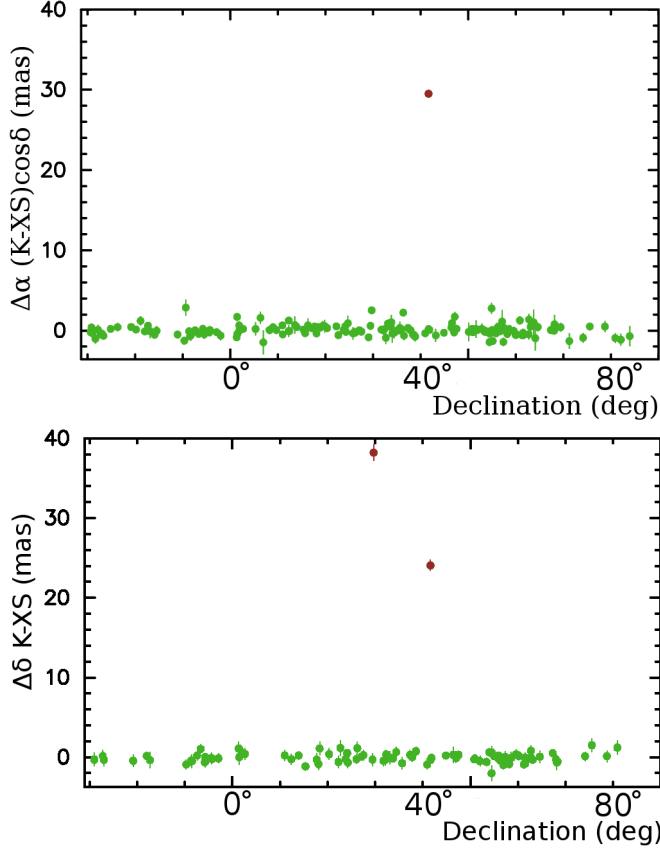


**Figure 16.** The differences in right ascensions scaled by  $\cos \delta$  (top) and declinations (bottom) from K band VGaPS versus S/X historical VLBA observations among 164 sources with uncertainties less than 2 mas. Positions of two sources differ significantly.

dimmer, 0.13 Jy, but more compact — 0.3 mas. We note that here and below in this section the total flux density reported for different source features is calculated as a sum of all CLEAN components representing the corresponding structure. The Gaussian components fit is being performed in the visibility plane.

It is evident that the VGaPS 24 GHz observations referred the position of the *weaker* A component, while the S/X observations referred the position of the C component. It is counter-intuitive. Since the component C is resolved, its contribution to fringe amplitude is small at long baseline projections. At short baseline projections the component C dominates, at long baseline projections the component A dominates. But since the partial derivative of group delay with respect to source position is proportional to the baseline length projection on the source tangential plane, the contribution of long baseline dominates in estimate of source position. According to Mantovanni et al. (2010), the total flux density of components A and C at 8.4 GHz in 2001 was 70 mJy and 1121 mJy respectively. This large difference between components' flux densities is also supported by the previous VCS1 observations of this object at S/X-bands. The component C is less resolved at 8.4 GHz and it dominates over A even at long baselines. Therefore, coordinate of a source at X-band are closer to the C component. We checked it directly, by suppressing observations at baselines longer than 800 km in a K-band trial solution. The position estimate became close to the X/S position. It is worth to note that the difference in position at K- and X-bands are  $29.2 \pm 0.4$  mas in right ascension and

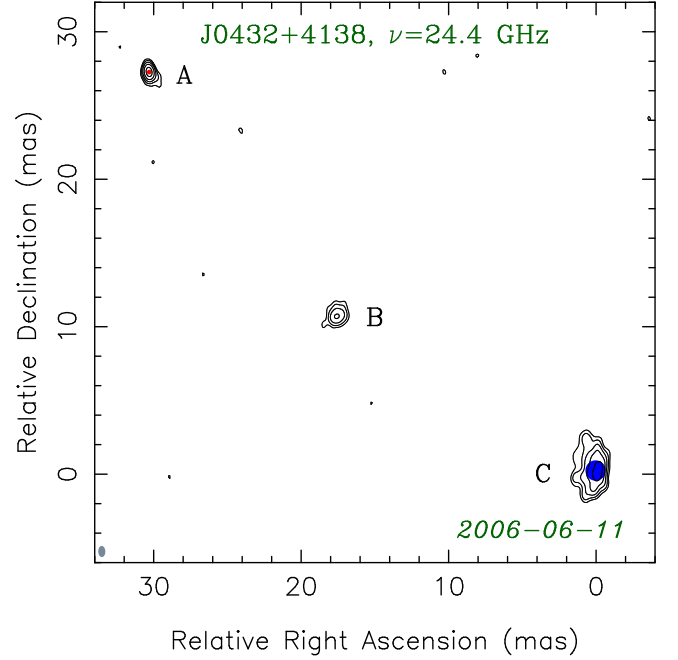


**Figure 17.** Naturally weighted K-band VGaPS CLEAN image of 3C119. The lowest contour of 4.1 mJy/beam is chosen at three times the rms noise, the peak brightness is 97 mJy/beam. The contour levels increase by factors of two. The dashed contours indicate negative brightness. The beam's full width at half maximum (FWHM) is shown in the bottom left corner of the images in grey. Red and blue spots indicate the positions and sizes (FWHM) of circular Gaussian model components for the features 'A' and 'C' respectively.

$24.1 \pm 0.4$  mas in declination, while the offset of the component A with respect to the component C at K-band is slightly larger:  $30.25 \pm 0.10$  mas and  $27.05 \pm 0.15$  mas. The K-band and X-band position is not exactly the position of components A and C, since in both solutions the contribution of the second component is small but not entirely negligible.

The nature of the difference in positions of J2020+2942 is similar. It was observed in VCS2 experiment on May 15, 2002 (Fomalont et al. 2003). It had 63 detections at S-band and 72 detections at X-band. Position of this source at S-band from analysis of only S-band data with applying the ionosphere contribution from the GPS TEC model shows a very large offset of  $0''.5$  with respect to the X-band position (refer to Table 11). The errors of the ionosphere contribution at S-band during the solar maximum affected position estimates considerably, however not to that extent. Comparison of positions of 130 sources with  $\delta > 0$  from the solution that used only S-band group delay observables with respect to the X/S solution in that experiment showed the differences in the range 2–7 mas. It is remarkable that the X/S position is away from *both* X and S-band positions, although intuitively we can expect them to be *between* X and S positions. This can be explained if to surmise that the source J2020+2942 has two components,  $0''.48$  apart, one of them visible at X-band, but not visible in the original S-band image, and another visible at S-band, but not at X-band. An ionosphere-free linear combination of X and S band observables is used in the X/S solution:  $(1 + \beta)\tau_{gx} - \beta\tau_{gs}$ , where  $\beta = 1/(\omega_x^2/\omega_s^2 - 1)$  as it follows from eqn. 27. In the case if position at S-band,  $\vec{k}_s$ , is shifted with respect to the X-band position vector,  $\vec{k}_x$ , the ionosphere



Table 11

Position difference of J2020+2942 at different frequencies with respect to its position at X-band

| Band | RA shift         |     | DEC shift         |     |
|------|------------------|-----|-------------------|-----|
| X    | $0.0 \pm 0.58$   | mas | $0.0 \pm 0.71$    | mas |
| S    | $25.77 \pm 4.11$ | mas | $478.79 \pm 4.39$ | mas |
| X/S  | $-2.29 \pm 0.54$ | mas | $-36.78 \pm 0.66$ | mas |
| K    | $0.25 \pm 0.41$  | mas | $1.45 \pm 0.70$   | mas |

**Note.** — The offset in right ascension is scaled by  $\cos \delta$ .

free linear combination can be written as

$$\tau_{if} = (1 + \beta) \tau_{gx}(\vec{k}_x) - \beta \tau_{gs}(\vec{k}_x) - \beta \frac{\partial \tau}{\partial \vec{k}}(\vec{k}_s - \vec{k}_x). \quad (32)$$

The first two terms correspond to the case of no offset between X and S band positions. Therefore, estimates of the source position from the ionosphere-free linear combination of observables will be shifted at  $-\beta$  with respect to the offset  $(\vec{k}_s - \vec{k}_x)$ , i.e. in the *opposite* direction. Parameter  $\beta$  was 0.076153 in the VCS2 experiment. Therefore, if our hypothesis that the X-band and S-band observations detected emission from two components is true, then the shift of X/S position with respect to the X-band position should be  $-1.96$  mas in right ascension and  $-36.46$  in declination, just within  $0.3$  mas from reported X/S positions! The K-band position is within  $1.5\sigma$  from the X-band position.

In order to check our hypothesis, we have re-imaged VCS2 observations of J2020+2942 in a wide field and have detected several previously unknown features ‘B’, ‘C’, ‘D’, on a distance up to about 500 mas from the dominating extended structure ‘A’ at S-band (Figure 18). The total flux density of the features A and D is 1.40 Jy and 0.09 Jy respectively. The feature A is significantly more extended than D. We have fitted two circular Gaussian components to the  $uv$ -data in order to determine positions of the features A and D. We note that the accuracy of position determination for the component A from the image is very poor since its structure being extended over at least 40 mas is not well represented by a single Gaussian component. The distance between Gaussian components A and D is 479 mas while positional difference in right ascension and declination is 25 and 479 mas respectively — in a very good agreement with independent astrometric measurements (Table 11).

X-band and K-band wide field imaging (Figure 19) did not reveal components with wide separation. We conclude from the astrometric analysis presented above that X- and K-band images represent the more compact component D. In this case we could also analyze its spectrum on the basis of simultaneous S/X-band observations. Its total flux density at X-band is found to be 0.25 Jy which provides the 2.3–8.6 GHz spectral index estimate  $\alpha = +0.8$  (flux density  $\propto \nu^\alpha$ ) — an indication of synchrotron emission with significant self-absorption. The features A, B, and C become too weak and/or too resolved that we could detect then in the snapshot VLBA images with a limited dynamic range and  $uv$ -coverage.

### 8.2. General comparison: uncertainties, systematic K-S/X-band difference, and the core-shift effect

Position differences for other objects do not show peculiarities. For instance, no declination dependent systematic differences similar to those reported by Lanyi et al. (2010) were found. The wrms of the differences is 0.46 mas in right ascension scaled by  $\cos \delta$  and 0.61 mas in declination. We

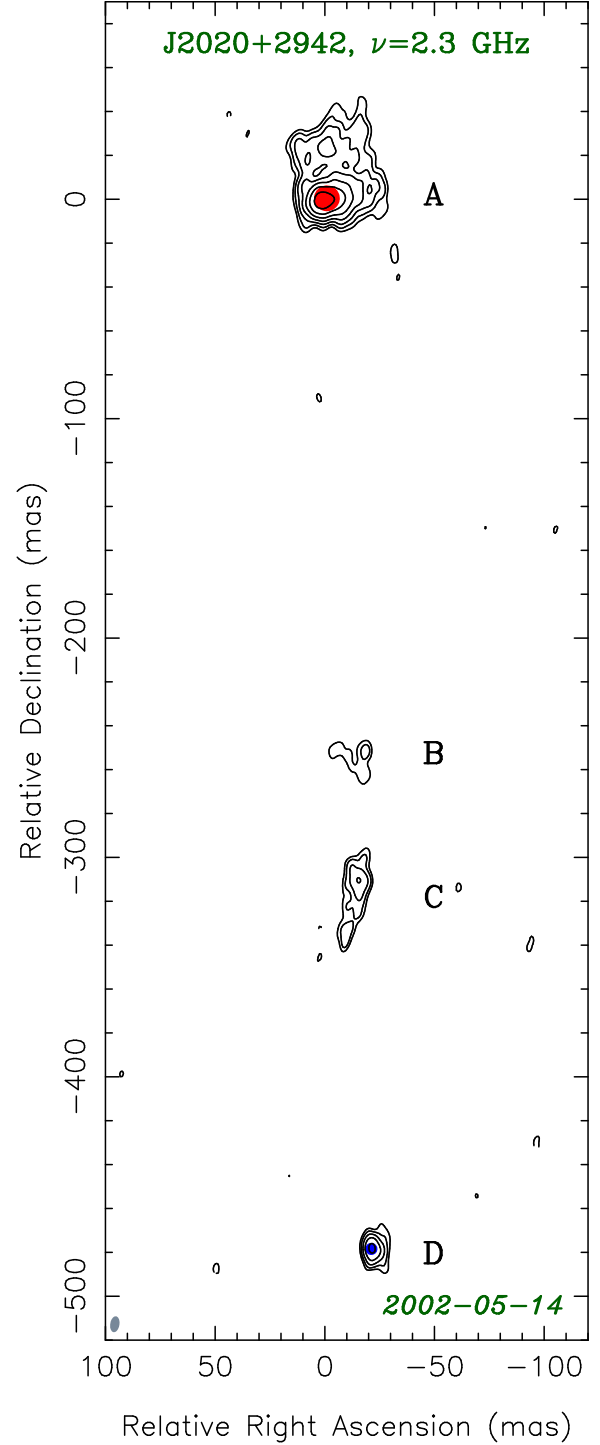


**Figure 18.** Naturally weighted S-band CLEAN image of 3C410 redone by us using VCS2 VLBA observations on 2002-05-14. The lowest contour of 2.5 mJy/beam is chosen at three times the rms noise, the peak brightness is 242 mJy/beam. The contour levels increase by factors of two. The dashed contours indicate negative brightness. The beam’s FWHM is shown in the bottom left corner of the images in grey. Red and blue spots indicate the positions and sizes (FWHM) of circular Gaussian model components for the features ‘A’ and ‘D’ respectively. It should be noted that feature A is very extended and the single Gaussian component does not represent it well.

have computed the normalized distances by dividing them by  $\sqrt{e_k^2 + e_{xs}^2}$ , where  $e_k$  is the projection of the error ellipse of

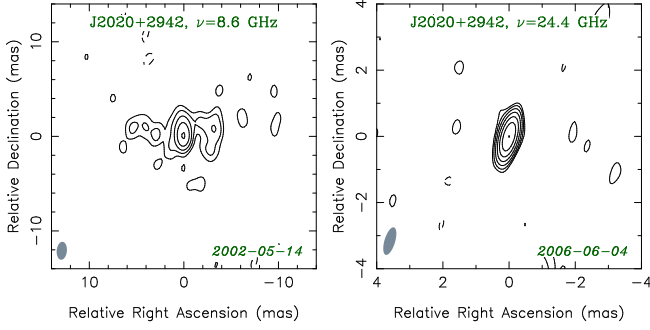


**Figure 19.** Naturally weighted X-band (left, VCS2 data) and K-band (right, this survey — VGaPS) CLEAN images of 3C410. The lowest contour at X- and K-band is 3.3 and 2.8 mJy/beam while the peak brightness is 56 and 178 mJy/beam respectively. On the basis of our analysis, we identify the feature presented in this Figure as feature ‘D’ from Figure 18.

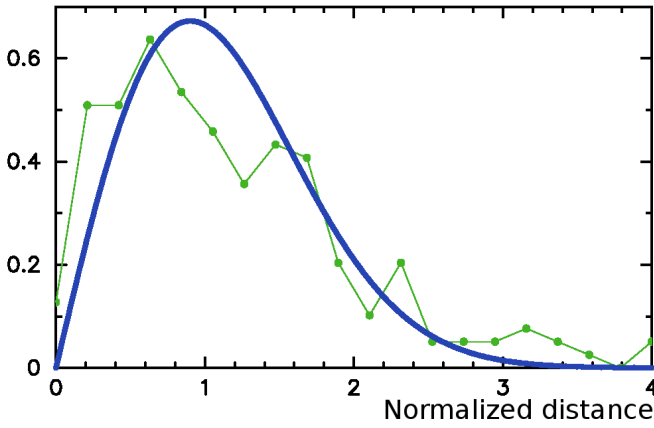


**Figure 20.** The empirical distribution of 190 normalized distances between K band position of target sources and their X/S positions (broken line) and the best fit Rayleigh distribution with  $\sigma = 0.90$  (solid thick line).

the K-band position to the direction of position difference and  $e_{XS}$  is the similar projection of the error ellipse of the X/S position. In the case if position errors from K-band and X/S catalogues are independent and Gaussian with the variance equal to reported uncertainties, the distribution of normalized distances will be Rayleigh with  $\sigma = 1$ . The average of the normalized distances over all sources, except J0432+4138 and J2020+2942, is 1.276, only 2% greater than the mean of the Rayleigh distribution,  $\sqrt{\pi/2}$ . However, a close examination of the distribution (see Figure 20) reveals a slight deviation of its shape from the shape of the Rayleigh distribution. The Rayleigh distribution that best fits the distribution of normalized distances has  $\sigma = 0.90$ . This is an indication of a deviation of parent distributions from Gaussian.

We can make several conclusions from this test. First, *on average* reported formal uncertainties are correct within several percents. Second, the effect of the core-shift is too small to contribute significantly on results of single-epoch surveys. According to Kovalev et al. (2008), the typical apparent core-shift is expected to be 0.4 mas between S- and X-bands. Porcas (2009) stressed that when the core-shift is proportional to  $f^{-1}$ , a source position derived from ionosphere-free linear combinations of X and S-band group delays is not sensitive to the core-shift and corresponds to a true position of the jet base. The  $f^{-1}$  core-shift dependence is expected for a conical jet with synchrotron self-absorption in the regime of equipartition between jet particle and magnetic field energy densities

(Lobanov 1998). If we assume that this is indeed the case for majority of the sources (see also Sokolovsky et al. 2011), the average core-shift between K-band and effective S/X positions is reduced to  $0.4 \cdot \frac{f_S f_X}{f_K (f_X - f_S)} = 0.06$  mas. Our observations would allow detecting the core-shift between positions from S/X and K-bands observables the 95% confidence level of a sample of 190 objects if the variance of the core-shift has been greater than 1 mas. VGaPS observations set the upper limit of this variance to 1 mas, which does not contradict to results of core-shift measurements and predictions.

## 9. SUMMARY

In the VLBA Galactic Plane Survey we detected 327 compact radio sources not previously observed with VLBI at 24 GHz in absolute astrometry mode. Half of them are within  $5^\circ$  of the Galactic plane; 206 of them were also observed and detected within the VCS or RDV programs at S/X bands in absolute astrometry mode. We determined K-band positions of all detected sources. The position uncertainties for all but one source are in the range from 0.2 to 20 mas with the median value of 0.9 mas. The quoted uncertainties account for various systematic effects and their validity within several percents was confirmed by comparison with independent X/S observations. The detection limit of our observations was in the range of 70–80 mJy. For the majority of detected sources parsec-scale images were produced and correlated parsec-scale flux density estimated. These results are presented in the form of the position catalog, calibrated image and visibility data in FITS format, and visual plots.

The new wide-band fringe search baseline-oriented algorithm for processing correlator output has been developed and implemented in the software *PLMA*. It has reduced the detection limit of observations by a factor of  $\sqrt{N}$ , where  $N$  is the number of IF’s, by determining group delays, fringe phases at the reference frequency, and phase delay rates from the coherent sum of the data from all IF’s. The new algorithm increased the number of detected target sources by a factor of 2.4 for this survey of weak objects near the Galactic plane. We validated the new algorithm by parallel processing of 1080 hours, over 0.6 million observations, using both the traditional AIPS approach and the new approach. The differences between source position estimates processed with the wide-field and with the traditional AIPS algorithms do not exceed 0.15 mas, which is satisfactory for any practical application.

We investigated possible systematic errors caused by errors in the ionosphere path delay derived from GPS TEC maps. We derived an empirical model of the ionosphere driven delay path errors. We found that for declinations  $> -20^\circ$  for 90% of the sources, mismodeling path delay caused source position errors of less than 0.05 mas. At declinations below  $-20^\circ$  these errors grow to 0.15 mas and for some sources may reach 0.5 mas.

Comparison of new K band VLBI positions with positions of 192 sources observed at S/X showed an agreement with the wrms of 0.46 and 0.6 mas in right ascensions and declination respectively, within reported position uncertainties for all but two compact steep spectrum sources J0432+4138 and J2020+2942. For these two objects, positional differences are about 40 mas. We showed that the reason of these differences is that for sources with complex extended structure positions were referred to different source details. These two objects demonstrate an existence of an overlooked source of errors in VLBI position catalogues that will be studied in de-

tail in the future. A 1 mas upper limit on an apparent core-shift effect between 8 and 24 GHz is found for the studied sample, in agreement with core-shift measurements and predictions by Kovalev et al. (2008), Sokolovsky et al. (2011), Porcas (2009).

# 10. ACKNOWLEDGMENTS

We would like to thank Leonid Kogan for fruitful discussions about hidden secrets of correlators. We used in our work the dataset MAI6NPANA provided by the NASA/Global Modeling and Assimilation Office (GMAO) in the framework of the MERRA atmospheric reanalysis project. This project was started when YYK was working as a Jansky Fellow of the National Radio Astronomy Observatory in Green Bank. YYK was supported in part by the JSPS Invitation Fellowship for Research in Japan (S-09143) and Russian Foundation for Basic Research (08-02-00545 and 11-02-00368). The National Radio Astronomy Observatory is a facility of the National Science Foundation operated under cooperative agreement by Associated Universities, Inc. The authors made use of the database CATS of the Special Astrophysical Observatory (Verkhodanov et al. 2005). This research has made use of the NASA/IPAC Extragalactic Database (NED, Eichhorn et al. 2002) which is operated by the Jet Propulsion Laboratory, California Institute of Technology, under contract with the NASA.

*Facilities:* VLBA (project code BP125), RATAN-600.

# REFERENCES

- Abdo, A. A., et al. 2010a, ApJS, 188, 405  
 Abdo, A. A., et al. 2010b, ApJ, 715, 429  
 Agnew, D. C. 1997, J. Geophys Res, 102, 5109  
 Beasley, A. J., Gordon, D., Peck, A. B., Petrov, L., MacMillan, D. S., Fomalont, E. B., & Ma, C. 2002, ApJS, 141, 13  
 Fey, A. L., et al. 2004, AJ, 127, 3587  
 Fomalont, E., Petrov, L., McMillan, D. S., Gordon, D., & Ma, C. 2003, AJ, 126, 2562  
 Eichhorn, G., et al. 2002, Ap&SS, 282, 299  
 1990, A&AS, 85, 805  
 Greisen, E. W. 1988, in Acquisition, Processing and Archiving of Astronomical Images, ed. G. Longo & G. Sedmak (Napoli: Osservatorio Astronomico di Capodimonte), 125  
 Honma, M., et al. 2003, PASJ, 55, L57  
 Kalnay, E. M., et al. 1996, Bull Amer Meteorol Soc, 77, 437  
 Kogan, L. 1993, NRAO VLBI Scientific memo, 6.  
<http://www.vlba.nrao.edu/memos/sci/sci06memo.pdf>  
 Kogan, L. 1995, NRAO VLBI Scientific memo, 9.  
<http://www.vlba.nrao.edu/memos/sci/sci09memo.pdf>  
 Kogan, L. 1998, Radio Sci., 33, 1289  
 Kopeikin S.M., Schäfer G. 1999, Phys Rev D, 60(12):124002  
 Kovalev, Y. Y. 2009, ApJ, 707, L56  
 Kovalev, Y. Y., Nizhelsky, N. A., Kovalev, Yu. A., Berlin, A. B., Zhekanis, G. V., Mingaliev, M. G., & Bogdantsov, A. V. 1999, A&AS, 139, 545.  
 Kovalev, Y. Y., Kovalev, Yu. A., Nizhelsky, N. A., Bogdantsov, A. B. 2002, PASA, 19, 83  
 Kovalev, Y. Y., et al. 2005, AJ, 2473  
 Kovalev, Y. Y., Lobanov, A. P., Pushkarev, A. B., Zensus, J. A. 2008, A&A, 483, 759  
 Kovalev, Y. Y., Petrov, L., Fomalont, E., Gordon, D. 2007, AJ, 133, 1236  
 Lanyi, G. E., et al. 2010, AJ, 139, 1695  
 Lobanov, A. P. 1998, A&A, 330, 79  
 Ma, C., et al. 1998, AJ, 116, 516.  
 Mantovani, F., Rossetti, A., Junor, W., Saikia, D. J., & Salter, C. J. 2010, A&A, 518, A33  
 Mathews, P. M. 2001, J. Geod Soc Japan, 47, 231  
 Matsumoto, K., & Takanezawa, T., Ooe, M. 2000, J. Oceanography, 56, 567  
 Matveenko, L. I., Kardashev, N. S., & Sholomitskii, G. B. 1965, Izvestia VUZov. Radiofizika, 8, 651 (English transl. Soviet Radiophys., 8, 461)  
 Murphy, T., et al. 2010, MNRAS, 420, 2403  
 Pearson, T. J., Shepherd, M. C., Taylor, G. B., & Myers, S. T. 1994, BAAS, 185, 0808  
 Petrov, L., & Ma, C. 2003, J. Geophys Res, 108(B4), 2190  
 Petrov, L. & Boy, J.-P. 2004, J. Geophys Res, 109, B03405  
 Petrov, L., Kovalev, Y. Y., Fomalont, E., Gordon, D. 2005, AJ, 129, 1163  
 Petrov, L., Kovalev, Y. Y., Fomalont, E., Gordon, D. 2006, AJ, 131, 1872  
 Petrov, L. 2007a, A&A, 467, 359  
 Petrov, L., Hirota, T., Honma, M., Shibata, S. M., Jike, T., & Kobayashi, H. 2007b, AJ, 133, 2487  
 Petrov, L., Kovalev, Y. Y., Fomalont, E., Gordon, D. 2007c, AJ, 136, 580  
 Petrov, L., Gordon, D., Gipson, J., MacMillan, D., Ma, C., Fomalont, E., Walker, R. C., & Carabajal, C. Jour. Geod., 2009, 83, 859  
 Petrov, L., Phillips, C., Bertarini, A., Murphy T., & Sadler E. M. 2011, MNRAS, in press, preprint (astro-ph/1012.2607)  
 Porcas, R. W. 2009, A&A, 505, L1  
 Ray, R.D. 1999, NASA/TM-1999-209478, Greenbelt, USA  
 Ros, E., Marcaide, J. M., Guirado, J. C., Sardón, E., & Shapiro, I. I. A&A, 2000, 356, 357  
 Ryan, J. W. & Clark, T. A. 1988 in Proceedings of The Impact of VLBI on Astrophysics and Geophysics; Proc 129th IAU Symp, Cambridge, MA. Ed: M. J. Reid and J. M. Moran, Kluwer Acad. Publ, p. 339  
 Schubert, S., et al. 2008, In Proceedings of Third WCRP International Conference on Reanalysis, Tokyo, V1-104.  
<http://wcrp.ipsl.jussieu.fr/Workshops/Reanalysis2008/Documents>  
 Sekido, M., Kondo, T., Kawai, E., & Imae, M. 2003, Rad. Sci., 38, 8  
 Sokolovsky, K. V., Kovalev, Y. Y., Pushkarev, A. B., & Lobanov, A. P. 2011, A&A, in press; arXiv:1103.6032  
 Sovers, O. J., Fanelow, J. L., Jacobs, C. S. 1998, Rev Modern Phys, 70, 1393  
 Schaer, S. 1998, Ph.D. thesis, Univ. Bern; accessible at <ftp://ftp.unibe.ch/aiub/papers/ionodiss.ps.gz>  
 Shepherd, M. C. 1997, in ASP Conf. Series, 125, Astronomical Data Analysis Software and Systems VI, ed. by G. Hunt & H. E. Payne (San Francisco: ASP), 77.  
 Thompson, A. R., Moran, J. M., & Swenson, G. W. 2001, Interferometry and Synthesis in Radio Astronomy, Wiley  
 Verkhodanov, O. V., Trushkin, S. A., Andernach H., Chernenkov, V. N. 2005, Bulletin SAO, 58, 118  
 Wrobel, J. M., Patnaik, A. R., Browne, I. W. A., & Wilkinson, P. N. 1998, A&AS, 193, 4004  
 Wrobel, J. 2009, NRAO eNews, vol. 2(11), 6